Article:

Lin, L., Miao, N., Wallace, G.G. et al. (2 more authors) (2021) Engineering carbon materials for electrochemical oxygen reduction reactions. Advanced Energy Materials, 11 (32). 2100695. ISSN 1614-6832

https://doi.org/10.1002/aenm.202100695

This is the peer reviewed version of the following article: Lin, L., Miao, N., Wallace, G. G., Chen, J., Allwood, D. A., Engineering Carbon Materials for Electrochemical Oxygen Reduction Reactions. Adv. Energy Mater. 2021, 2100695., which has been published in final form at https://doi.org/10.1002/aenm.202100695. This article may be used for non-commercial purposes in accordance with Wiley Terms and Conditions for Use of Self-Archived Versions.

DOI: 10.1002/ ((please add manuscript number))
Article type: Progress report

Engineering Carbon Materials for Electrochemical Oxygen Reduction Reactions

Liangxu Lin[#,*] *Naihua Miao*,[#] *Gordon G. Wallace, Jun Chen*,[*] *and Dan A. Allwood*[*]

Dr Liangxu Lin, Prof. Gordon G. Wallace, Prof. Jun Chen
ARC Centre of Excellence for Electromaterials Science, Intelligent Polymer Research Institute, Australia Institute for Innovative Materials (AIIM), Innovation Campus, University of Wollongong, Squires Way, North Wollongong 2519, Australia
Email: liangxu@uow.edu.au (LL); junc@uow.edu.au (JC)

Prof. Naihua Miao,
Center for Integrated Computational Materials Engineering, School of Materials Science and Engineering, Beihang University, Beijing 100191, China

Prof. Dan A. Allwood,
Department of Materials Science and Engineering, University of Sheffield, Sheffield S1 3JD, United Kingdom
Email: d.allwood@sheffield.ac.uk

[#] Contributed equally to this work

ABSTRACT: The electrochemical oxygen reduction reaction (ORR) is the key energy conversion reaction involved in fuel cells, metal-air batteries and hydrogen peroxide production. Proliferation and improvement of the ORR requires wider use of new and existing high performance catalysts; unfortunately, most of these are still based on precious metals and become uneconomical in mass-use applications. Recent progress suggests that low cost and durable carbon materials can potentially be developed as efficient ORR catalysts. Significant efforts have been made in discovering fundamental catalytic mechanisms and engineering techniques to guide and enable viable regulation of both the ORR activity and selectivity of these carbon catalysts. Starting from the fundamental understanding, this report reviews recent progress in engineering carbon materials from exotic chemical doping to intrinsic geometric defects for improved ORR. On the basis of both theoretical and experimental investigations reported so far in this area, future improvements in carbon catalysts are also discussed, providing useful pathways for more efficient and reliable energy conversion technologies.

Keywords: carbon materials; oxygen reduction reaction; electronic structure; adsorption energy; density functional theory

1. Introduction

The electrochemical oxygen reduction reaction (ORR) is one of the most important energy conversion reactions to involve O_2 and H_2O, and can be used in proton-exchange membrane fuel cells (PEMFCs), rechargeable metal-air batteries and the production of hydrogen peroxide (H_2O_2).[1-4] In PEMFCs and metal-air batteries, the ORR starts from the adsorption of O_2 molecules at the cathode, electrochemical activation of the O-O bond and then the formation of O-containing groups such as OOH*, O* and OH*. In this way, O_2 is reduced by the electrons (**Figure 1a**).[4] The efficiency of these energy devices is usually determined by that of the ORR process. However, the strong bond energy of O-O (498 kJ mol^{-1}) means that the ORR at the electrode is not easy, especially compared to the hydrogen oxidation reaction (HOR: $H_2 \rightarrow 2H^+ + 2e^-$) at the anode of hydrogen-oxygen fuel cells (**Figure 1a**). Improvement of O-O bond activation and cleavage with catalysts is therefore highly important in developing efficient energy storage and conversion systems as well as fast and efficient chemical production techniques.

Nevertheless, in industry, the most common ORR catalysts are still Pt-based materials, which are prohibitively expensive for wider application (**Figure 1b**).[5] There is a pressing need to explore alternative electrocatalysts that are cheap and stable. Significant efforts have been made to develop alternative materials (*e.g.,* transition metal oxides, alloys, metal-organic frameworks/MOFs, single atom catalyst) and investigate their catalytic mechanisms,[6-12] but challenges remain. In 2009, Dai's group reported using doped carbon nanotubes (CNTs) to catalyze ORR that exhibited better catalytic efficiency than commercial Pt/C electrodes in alkaline media.[13] It should be noted that, in alkaline media, the hydroxide conducting polymeric membranes (*e.g.* in anion exchange membrane fuel cells) are unstable and have poor resistance to CO_2, while the overpotentials for hydrogen oxidation are also high.[14-16] Compared to metal-based catalysts, carbon materials have significant merits of outstanding anti-corrosion performance and electrochemical durability, as well as the possibility of low-cost manufacture. This combination means that carbon materials are seen as highly promising candidates to replace precious metals as ORR. In the years following Dai's pioneering work, various other doped carbon materials were further developed and their catalytic mechanisms investigated.[17-22] Some more recent studies explored this further and suggested that active intrinsic carbon structural defects are associated with efficient ORR catalysis (**Figure 2b**).[23-

26] Although great progress has been achieved on this topic, the origin and mechanism of the ORR activity are still not fully clear. Beyond the catalytic activity, no pattern has been established in the selectivity between the two-electron/2e$^-$ and four-electron/4e$^-$ processes of reported carbon materials.[17-33]

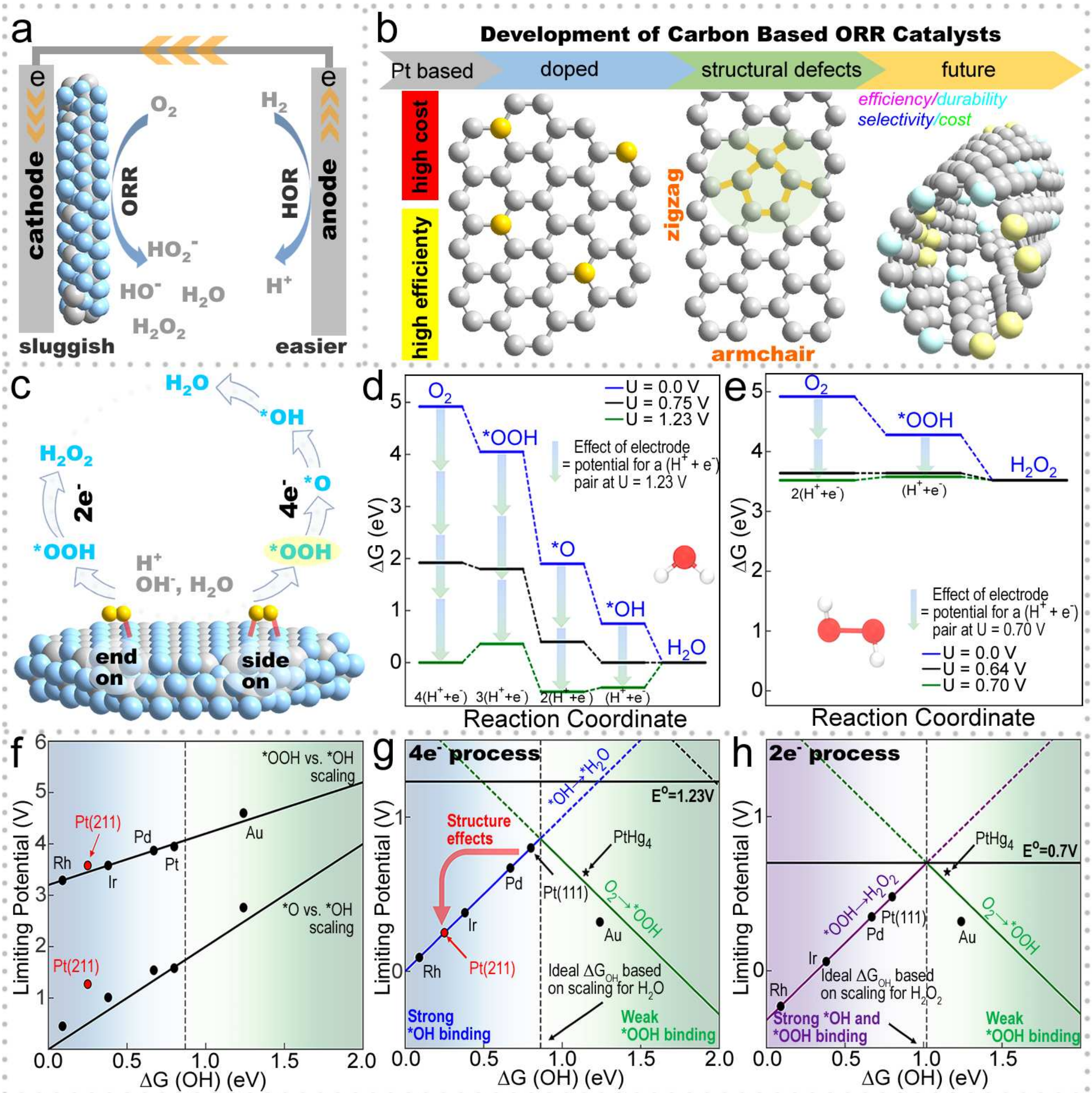

Figure 1. a) Schematic of the ORR used for energy conversion in fuel cells; b) The development of carbon-based ORR catalysts over time; c) Schematic shows end on and side on adsorption on the catalyst, and ORR pathwats with 2 and 4e$^-$ electron transfer (the 4e$^-$ dissociative process has no *OOH involved); d, e) Free energy diagram for the 4e$^-$ associative ORR on Pt(111) (d) and 2e$^-$ associative ORR on $PtHg_4$; f) Scaling relationships for the chemisorption energies of *OOH and *O against the *OH on the (111) of different metals [ΔG (*OOH) = ΔG (*OH) + 3.2; ΔG (*O) = 2ΔG (*OH)]; g) Volcano plot of limiting potentials as a function of *OH free energy for the 4e$^-$ process, highlighting the regions of strongly bound *OH (solid blue line) and weakly bound *OOH (solid green line); h) Volcano plot of limiting potentials as a function of *OH free energy for the 2e$^-$ process, highlightling the regions of strongly bound *OH (solid purple line) and weakly bound *OOH (solid green line). In f, g and h, the color gradient represents the strong *OH and weak *OOH binding regions. (d)-(h) are reproduced with permission.[34] Copyright 2018, American Chemical Society.

In this report, we explore how the catalytic efficiency and selectivity of carbon materials supporting the ORR might be developed to enhance the performance and viability of energy conversion technologies. We first present the fundemental mechanism of the ORR, and summarize viable approaches used to engineer carbon materials to regulate both the catalytic activity and selectivity. We then introduce the principles that underpin carbon materials as ORR catalyst before discussing their future prospects for highly efficient and selective ORR.

2. Fundamentals of ORR

2.1 Reaction Pathways

ORR has two reaction pathways of 2e$^-$ (conversion to H_2O_2) and 4e$^-$ (conversion to H_2O) reductions, related to dissociative and associative processes, and that depends on the adsorption mode, activation and cleavage barrier on the catalyst surface.[12,34,35-37] Although the 2e$^-$ reduction is not of assistance in fuel cells, it can be used for the production of H_2O_2 and developed for relevant applications, such as electrochemical degradation of organic pollutants and the sterilization of water systems. In acidic solution, the 4e$^-$ reduction of O_2 can be expressed with the following reactions:[12,36,37]

The direct dissociative pathway:

- $O_2 + 2^* \rightarrow 2^*O$ (Equation 1)
- $2^*O + 2H^+ + 2e^- \rightarrow 2^*OH$ (Equation 2)
- $2^*OH + 2H^+ + 2e^- \rightarrow 2H_2O + 2e^*$ (Equation 3)

and the indirect associative pathway:

- $O_2 + {}^* \rightarrow {}^*O_2$ (Equation 4)
- ${}^*O_2 + H^+ + e^- \rightarrow {}^*OOH$ (Equation 5)
- ${}^*OOH + H^+ + e^- \rightarrow H_2O_2$ (Equation 6)
- ${}^*OOH + H^+ + e^- \rightarrow {}^*O + H_2O$ (Equation 7)
- ${}^*O + H + e^- \rightarrow {}^*OH$ (Equation 8)
- ${}^*OH + H^+ e^- \rightarrow H_2O + {}^*$ (Equation 9)

In alkaline solution, the presence of OH$^-$ causes the H$^+$ (or hydronium ion) to become H_2O, although the intermediates of HOO*, O* and *OH (**Figure 1c**) still occur, which is in contrast to the 2e$^-$ process only having HOO* as an intermediate.[35] Activation of the O-O bond can be realized by bonding with catalytic sites. The specific electronic environment around the active catalytic site can also change the electronic distribution of a O-O species and affect its activation. The O-O can be side adsorbed on the active site (side-on adsorption) or end-on a single active site (**Figure 1c**), which weakens the O-O bond and promotes the dissociative process (the activation and cleavage of the O-O bond). However, a strong interaction with many metal catalysts between the active catalyst sites and O_2 hinders the removal of the H_2O_2 formed in both the dissociative (Equation 1, 2) and associative process (Equation 4, 5, 6) and prevents the further reduction of the *OOH to form H_2O (Equation 3, 7, 8, 9). In end-on adsorption, if the binding is not strong enough to dissociate O_2, the two-electron reduction will be the favored route and result in an end product of H_2O_2, as observed at defect sites in many carbon materials.[37]

2.2 Free Energy

In a catalyst with weak surface activity, the O_2 adsorption step may need to be considered as a possible rate-limiting step to compare with the adsorption of ORR intermediates (HOO*, O* and *OH). However, to simplify the analysis, Nørskov *et al.* treated the adsorption of O_2 on a metal catalyst surface as a chemical step that is unlikely to be the rate-limiting process of ORR, assuming a simple electron-proton transfer process from hydronium to oxygen.[34] The free energy of the intermediates (*OOH, *O, *OH) can then be considered the basis with which to understand ORR mechanism. According to calculations, the activation energy barriers of each reaction are potential dependent, which is mainly due to the free energy of intermediates.[35] With the computational hydrogen electrode (CHE) model,[34,38] the adsorption free energy of a reaction intermediate (ΔG, with *n* proton-electron pairs) can be expressed as a function of the potential by:

$$\Delta G = \Delta E_{elc} + \Delta E_{w} + \Delta E_{field} + \Delta ZPE - T\Delta S - neU \quad \text{(Equation 10)}$$

where ΔE_{elc}, ΔE_w, ΔE_{field}, ΔZPE, $T\Delta S$ and $-eU$ are the density functional theory (DFT) calculated binding (adsorption) energy, effects of adsorbate solvation, electric field effects, zero-point energy, entropic corrections, and the free energy of a single proton-electron pair (U is the electrode potential versus a reversible hydrogen electrode [RHE]). On this basis, Nørskov *et al.* plotted the free energy diagram for the $4e^-$ associative ORR on Pt (111) (**Figure 1d**) and $2e^-$ one on $PtHg_4$ (**Figure 1e**).[34,35] In the $4e^-$ ORR process and at the equilibrium potential of 1.23 V (**Figure 1d**), the reductions of O_2 to *OOH and *OH to H_2O all have to overcome a free energy barrier. The maximum potential (thermodynamic limiting potential) where both of these reactions are exergonic (so large ORR current densities occur) is calculated to be about 0.8 V on Pt (111). One parameterization of ORR activity is the theoretical potential calculated as the equilibrium potential subtracted by the limiting potential; here this is around 0.43 V. In the $2e^-$ ORR process on $PtHg_4$ (**Figure 1e**), the formation of *OOH is slight increase in free energy at an equilibrium potential of 0.7 V. The thermodynamic limiting potential is 0.63, indicating that the theoretical potential in this case is 0.07 V.[34]

2.3 Scaling Relationship and Volcano Plots

The above discussed theoretical overpotential of the associative ORR is a function of the binding free energy of the three intermediates (*OOH, *O and *OH), which are strongly correlated and change monotonically for different catalysts.[34,39-41] These binding energies and limiting potentials are linearly correlated because the intermediates all bind with the catalyst through the O atom. The following equation can then be applied to describe the binding energy scaling relation between different intermediates (1 and 2):[34,42]

$$\Delta G_2 = A_{1,2} \times \Delta G_1 + B_{1,2} \quad \text{(Equation 11)}$$

where the slope $A_{1,2}$ and the intercept $B_{1,2}$ depend on the electron-counting rule, while the intercept also depends on the nearest-neighbor-counting rules. As result, the slope of the scaling relation of *OOH *vs* *OH and *O *vs* *OH are around 1 and 2, respectively to satisfy electron-counting rules (*e.g.,* the octet rule where the required electron number on the O atom in *OOH (*OH) and *O is 1 and 2, respectively). The binding free energy of *OOH and *OH, therefore, have the scaling relation with the equation of ΔG (*OOH) = ΔG (*OH) + 3.2 ± 0.2 eV, which occurs at most catalyst surface (**Figure 1f**).[12,34] Such scaling relation limited the availability of catalysts with high limiting potential for the 4e$^-$ ORR process. It also means that the ORR can be independently described by the *OH binding free energy (also represented as ΔG_{OH}).[34,43] Since the theoretical overpotential is a function of binding free energies of the three intermediates, the limiting potential can be calculated from the *OH binding directly based on the above scaling relations. **Figure 1g** shows the results of this calculation for the 4e$^-$ process in which is known as a 'volcano' plot, due to the crossed relations for *OH and *OOH binding. Norskov *et al.* concluded from these plots:[34] 1) for catalysts that bind strongly with the *OH, the reaction of *OH→H_2O is potential limiting (the solid blue line in **Figure 1g**); and 2) for catalysts that show weak binding, O_2→*OOH is potential limiting (solid green line in **Figure 1g**). This understanding creats a route to use various engineering strategies of catalyst materials, such as edge strucrure, strain, boundary modification and doping, to design regulation of the binding strength of a catalyst and, therefore, to reach the minimun theoretical overpotential (~0.37 V) of the 4e$^-$ process.

For the 2e$^-$ ORR process, since *OOH is the only intermediate involved in the reaction, its formation or the removal becomes the only rate-limiting step (without the consideration of O_2 adsorption). On the basis of above scaling relations, a similar volcano plot (**Figure 1h**) can also be prepared to show the relationship between the limiting potential and the *OH binding free energy. For catalysts with strong binding abilities, the desorption of *OOH to form H_2O_2 will be the rate-limiting reaction step. By contrast, if the binding between O_2 and the catalyst is relatively weak, the activation of the O_2 and the reaction of the O_2→*OOH will be the rate limiting step. Optimal binding ability of the catalyst, in principle, can be reached by suitable regulation of the materials, giving potentially a zero overpotential like that in the hydrogen evolution reactions (HER) (**Figure 1h**).[44,45]

2.4 Reaction Rate and Selectivity

Microkinetic modeling of the ORR suggests that the ORR is intrinsically fast but becomes limited by O_2 diffusion at low potential (< 0.65 V versus RHE) and by O_2 adsorption at high potentials (~0.9 V versus RHE).[34] In practice, the reaction rate of the ORR also depends on the number of the active sites, temperature and the pH of electrolytes.

Selectivity between the $2e^-$ and $4e^-$ pathways is determined by the competing *OOH reactions that yield to H_2O_2 and H_2O (Eqs. 6 and 7).[2,46] As suggested by the Eq. 7, the key to suppress the $4e^-$ process is to avoid the dissociation of the O-O bond in *OOH. We can use the scaling relations discussed above to predict that catalysts with strong binding abilities are unsuitable for the selection of $2e^-$ pathway. Recent developments suggest that carbon materials may be interesting in this regard, given their inactive graphite plane and highly active N-doped states of CNTs well suited for the $4e^-$ process. Regulation of the electronic states of carbon materials between pristine graphite and CNTs is possible. This regulation may be achieved by, for example, introducing dangling bonds, or tuning the density of states (DOS) around the Fermi level and electronic distributions near active regions (*e.g.* by strain, geometric defects and polarized edge states).[47]

3. Engineering Strategies of Carbon Materials for ORR

With all the above understanding, we discuss below the development of carbon catalysts and engineering strategies towards the improved and controlled catalysis, including mainly the chemical doping and defect engineering. Other strategies such as monatomic catalyst and hybrid/heterostructures will not be discussed in this report as their catalytic activities are mainly raised from exterior materials rather than the carbon structures.

Understanding of the ORR mechanism of engineered carbon materials are mainly based on the DFT investigations which suggested only weak physisorption (bound by dispersive van der Waals forces, no charge transfer happens) of O_2 on the CNT and graphene surface.[48-51] In the DFT calculation reported by Giannozzi *et al.*, the graphene and semiconducting single-walled CNTs (SWCNTs) have the binding energy of 0.1 and 0.08 eV, respectively to the triplet O_2.[50] Veiga *et al.* further calculated the binding energy of O_2 at both the zigzag and armchair graphene nanoribbons.[51] Among all investigated structures (**Figure 2a,b**), the H-terminated zigzag structure is the only one which can chemically interact (bound by the formation of a chemical bond, charge transfer happens) with the O_2. The weak binding ability to O_2 of the plane of graphene layer and semiconducting CNTs explains why the carbon materials have to be suitably regulated (*e.g.* chemical doping) to enable the ORR catalysis.

3.1 Chemical Doping

3.1.1 N doping

In 2009, Dai's group reported the N-doped CNTs (**Figure 2c-e**) which exhibited superior ORR performance (*e.g.* the higher steady-state diffusion current and better durability) over that of Pt/C catalyst in 0.1 M KOH electrolyte.[13] The electron transfer number for one oxygen molecule conversion was calculated as close to four at half-wave potential, suggesting a relatively high binding energy between the O_2 and N-doped CNTs (**Figure 1g-h**). The C atoms surrounding the N dopant (electronegativity of C: 2.55; electronegativity of N: 3.04) have higher positive charge density than others (**Figure 2f**), which changed the O_2 chemisorption from the end-on (Pauling model) to a side-on model (Yeager model, see **Figure 1c**), and weakened the O-O bonding to facilitate ORR.[13] The detailed mechanism was actually not really clear at that time considering the existence of various possible N-doped structures such as pyridinic, graphitic and pyrrolic N.[31,52-59]

Based on both experiments and DFT studies, various results have been then reported to discuss how carbon materials can be activated for ORR by N doping.[52-59] These N doped carbon materials are usually too complex (i.e., the effects from geometric defects have been overlooked in many early studies),[30,52,54,56,57,58,60-64] and the ORR between different N-doped structures are difficult to be precisely distinguished. In particular, many geometric defects (e.g., edge, strain, crystal distortion) of pristine carbon materials are actually active for ORR (will be further discussed in **Section 3.2**), giving great uncertainty of the experimental results. Nevertheless, the DFT investigations involved in these works have provided a relatively comprehensive understanding on the trend of ORR catalysis.[55,59,61, 65-69] For example, Henkelman *et al.* discussed the ORR on pure and N-doped graphite materials (model: five layers of graphene) in detail (**Figure 2g-i**).[70] The C atoms close to the edge with 3C and 2C1N coordination have only weak binding ability to O_2, which were directly excluded for the ORR together with the unusual pyrrolic N structure (N bonded to two C and one H in a five-membered ring). Their investigation suggested that the ORR activity of various N doped structures follows the order of zigzag edge > N_p-Z > N_g-Z > N_p-A > N_g-A > N_g-B > armchair edge at pH =1, and the order of zigzag edge > N_p-A > N_g-Z > N_g-B > armchair edge at pH = 13 (structures are defined in **Figure 2h**, also see descriptions below). Especially, the DFT calculation gave key findings of:[70]

- **Basal plane**: without graphitic N doping (Ng), the carbon atoms at basal plane are unable to chemically bind with O_2 and ORR intermediate; The Ng can improve the binding ability of the neighbouring C atoms (Ng-B, structure 2 in **Figure 2i**) slightly, which has the theoretical onset potential (where the ORR starts) of 0.08 and 0.39 V (*vs.* RHE) at pH = 1 and 13, respectively. The pH-dependent activity is attributed to the potential-dependent binding abilities to ORR intermediates (increase with increasing electrode potential).
- **Zigzag edge**: the zigzag edge (structure 1 in **Figure 2i**) of pristine graphite is highly active for ORR in both acid (theoretical onset potential of 0.6 V *vs.* RHE at pH = 1) and alkaline medias (theoretical onset potential of 0.7 V *vs.* RHE at pH = 13, **Figure 2g-h**). The reduction of *OH to H_2O (Equation 3) is the potential-limiting step in

acidic media, while the *OH formation step (Equation 2) determines the onset potential in alkaline media.

- **Armchair edge**: compared to the zigzag edge, the two under-coordinated C atoms at armchair edge (structure 5 in **Figure 2i**) have relatively strong C-C bonding (bond length of 1.37 Å *vs.* 1.41 Å of zigzag C-C), giving weak binding abilities to the ORR intermediate and poor activities in both acidic and alkaline medias (**Figure 2h**).
- **Pyridinic N-doped zigzag edges (Np)**: the Np (structure 3 in **Figure 2i**) can directly occupy the most active zigzag edge and deactivate the neighboring zigzag C site (Np-Z, **Figure 2i**), giving reduced theoretical onset potentials of 0.4 and 0 V (*vs.* RHE) at pH of 1 and 13, respectively (**Figure 2h**). However, the ORR activity is still higher than that of the armchair structures.
- **Pyridinic N-doped armchair edges** (structure 6 in **Figure 2i**): the Np (C-N) weakens the C=C bond, which correspondingly improves the ORR activity of the neighboring C site (armchair C, Np-A, **Figure 2i**), giving theoretical onset potential of ORR as around 0.63 and 0.3 V (*vs.* RHE) in alkaline and acidic medias, respectively (**Figure 2h**).
- **Graphitic N near zigzag edge** (Ng, structure 4 in **Figure 2i**): in this case, the theoretical ORR onset potentials of the neighbouring zigzag C (Ng-Z) was predicted as 0.36 and 0.56 V (*vs.* RHE) at pH = 1 and 13, respectively (**Figure 2h**), which are all lower than the pristine zigzag structure. Such negative affect on the ORR activity also slightly works on the next nearest-neighboring zigzag C atom.
- **Graphitic N near armchair structure** (structure 7 in **Figure 2i**): the bond length of armchair C-C is reduced upon the graphitic N doping at the nearest C atom. Therefore, the binding ability of the nearest (to the graphitic doping position) armchair C to O_2 (N_g-A) is too weak to activate the ORR.

- **Synergy between N_g and N_p:** electron transfer from the N_g to N_p improves the catalytic activity at the armchair position (**Figure 2i**).

These results are interesting by suggesting the highly active zigzag edges and detailed effect of N doping on the ORR activity. Nevertheless, in most cases, the edge structure of carbon materials is oxidized and needs to be studied further (see **Section 3.2.1**). Besides, the modeling did not considered the competitive associative $2e^-$ reaction pathways, which may only need relatively weaker binding ability compared to that of the dissociative $4e^-$ reactions (see **Section 2.4**).

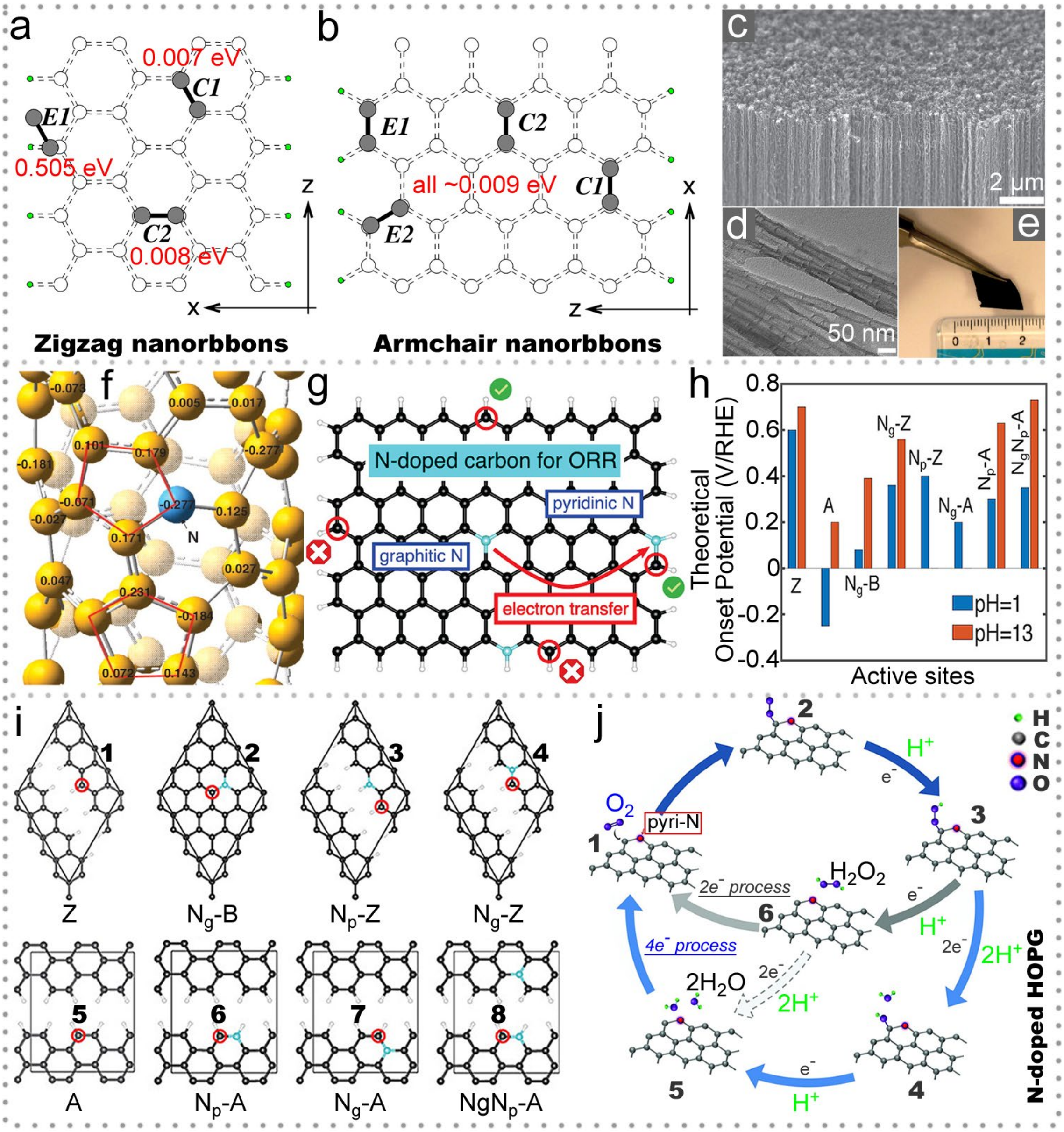

Figure 2. a,b) Structural model and O_2 (triplet state) adsorptions on the zigzag (a) and armchair graphene nanoribbons (b) with H terminations at the edge. Reproduced with permission.[51] Copyright 2008, AIP publishing; c-e) Scanning electron microscopy/SEM (c), transmission electron microscopy/TEM images (d) and digital photograph (e) of the N-doped CNTs; f)

The calculated charge density distribution of the N-doped CNTs. (c)-(f) are reproduced with permission.[13] Copyright 2009, AAAS; g) Diagram shows the structures of the graphitic N (Ng) and pyridinic N (Np) in graphene and their synergistic effect in ORR; h) Theoretical onset potential for different active sites at pH of 1 and 13; i) Atomic structures of different active sites (A, Z and B mean armchair and zigzag edges and basal plane, respectively). In g and i, the C, N and H are represented by black, cyan and white, respectively. The sites to bind with ORR intermediate are marked as red circles. Figures (g)-(i) are reproduced with permission.[70] Copyright 2020, American Chemical Society; j) ORR pathways on N-doped carbon materials. Reproduced with permission.[59] Copyright 2016, AAAS.

In 2016, Nakamura *et al.* prepared the highly oriented pyrolitic graphite (HOPG) with well-defined π conjugation and controlled N species.[59] This preparation allowed the comparison between graphite and various N-doped graphite structure, giving the ORR catalytic activity of pyridinic N-dominated HOPG > graphitic N-dominated HOPG > edge patterned HOPG (without N doping) at pH = 13. The characterization suggested that the C atoms near pyridinic N are ORR active sites, which have a localized DOS in the occupied region near Fermi level, and act as Lewis bases to adsorb O-species.[59,71,72] Nakamura *et al.* proposed a possible mechanism for the N-doped HOPG with both associative (steps 1→2→3→4→5) and dissociative processes (steps 1→2→3→4→6, acidic media, **Figure 2j**). In the associative process, the adsorbed O_2 at the active C sites is protonated (two protons), giving the breakage of the O-OH bond and formation of OH species. One proton further reacts with the remained –OH to generate H_2O. In the dissociative processes, the O_2 is initially protonated to form *OOH (steps 1-3) which is then reacted with another proton to form H_2O_2 (steps 3 → 6, **Figure 2j**). The H_2O_2 is then re-adsorbed and reduced to the H_2O (step 6 → 5, **Figure 2j**). These proposed reaction routes match well with above equations 1-7. Nevertheless, according to the DFT calculations,[70] the ORR catalysis of pyridinic N structure is still not as good as that on the pure zigzag structure. The catalytic activity of the edge in the HOPG may be under-estimated,[59] assuming the small number of the edge structure and the existence of relative inactive armchair edges. In many ring-disk electrodes (*e.g.,* the glassy carbon disk), besides the higher ORR current background, the onset potential is also higher than that of all the above N-doped HOPG materials.[73] Besides, the $4e^-$ dissociative process may be not the case in the HOPG when the measured and calculated onset potential is too low and far away from the equilibrium potential of 1.23 V (versus RHE, *e.g.,* around 0.4 V in the pyridinic N-dominated HOPG, close to the theoretical one).[59,70] The binding ability of these graphite materials may be still too weak when comparing with that on the N-doped CNTs which has the 4e$^-$ process.[13] This is reasonable as the C-C/C=C bond length in CNTs is usually larger than that in pure graphite structures.[74-76] According to Henkelman's research, the longer bond length means a weaker C-C bonding and an enhanced binding strength to ORR intermediates.[70] The higher surface energy of CNTs (from the surface curvature and defect)[77-79] over that of the basal graphite may also improves the binding ability to O_2 (will be further discussed in **Section 3.2**).

3.1.2 B doping

Since the N doping can regulate the electronic distribution of nearby C atoms, similar elements such as B, S and P with different electronegativity to that of C have also been used to functionalize carbon materials toward the improved ORR.[17,80-87]

In 2011, Hu *et al.* investigated the impact of B doping on the ORR activity of CNTs.[17] **Figure 3a and b** show the contour plots of spin up and spin down highest occupied molecular orbital (HOMO) of physisorbed O_2 on the pristine CNT (5,5, armchair), respectively. Upon the adsorption of O_2 on CNTs, the orbital overlap only happens when the wave function has the same sing with small negative charge transfer (-0.1e, **Figure 3a**). Otherwise for the wave functions with different signs, the antibond will form in the system and repel O_2 away from the CNT (**Figure 3b**). The CNT can be treated as a typical spin-singlet system, while the O_2 triplet electron configuration has two unpaired electrons with identical spins.[17] The orbital mismatch between uncharged CNTs and the ground state triplet O_2 means that the O_2 cannot be chemically adsorbed on the CNTs. However, in the case of the B doping (BC_3 coordination, sp^2-like hybridization in B-C σ bonds, **Figure 3c)**, the B-C σ bonds are considerably polarized due to the electronegativity difference between C (electronegativity: 2.55) and B (electronegativity: 2.04). Such polarization gives a 0.56 e positive charge on the B atom (**Figure 3c**), benefiting the chemical adsorption of O_2 molecule (slightly negatively charged upon approaching CNTs). This ORR activation model is different with that of N doping (**Figure 2f**), while the B dopant is the active site to adsorb O_2 and ORR intermediates. **Figure 3d** shows the process of O_2 adsorption on B-doped CNTs, proposed by Hu *et al.*[17] During this process, the lowest unoccupied molecular orbital (LUMO) of a triplet O_2 (molecular orbitals 2, **Figure 3d**) overlaps with the protruding lobe spin-down HOMO of B-doped CNT (molecular orbitals 1, **Figure 3d**) to form an end-on adsorption (molecular orbitals 3, **Figure 3d**) with the adsorption distance of 1.55 Å. The adsorption free energy of this process was calculated as -0.11 eV, and therefore is an exothermic step. Charge transfer (0.45 e, from the C through the B bridge) from B to O_2 happens with the elongation of the O-O bond length from 1.21 Å to 1.32 Å, and the O-O is activated for the ORR.

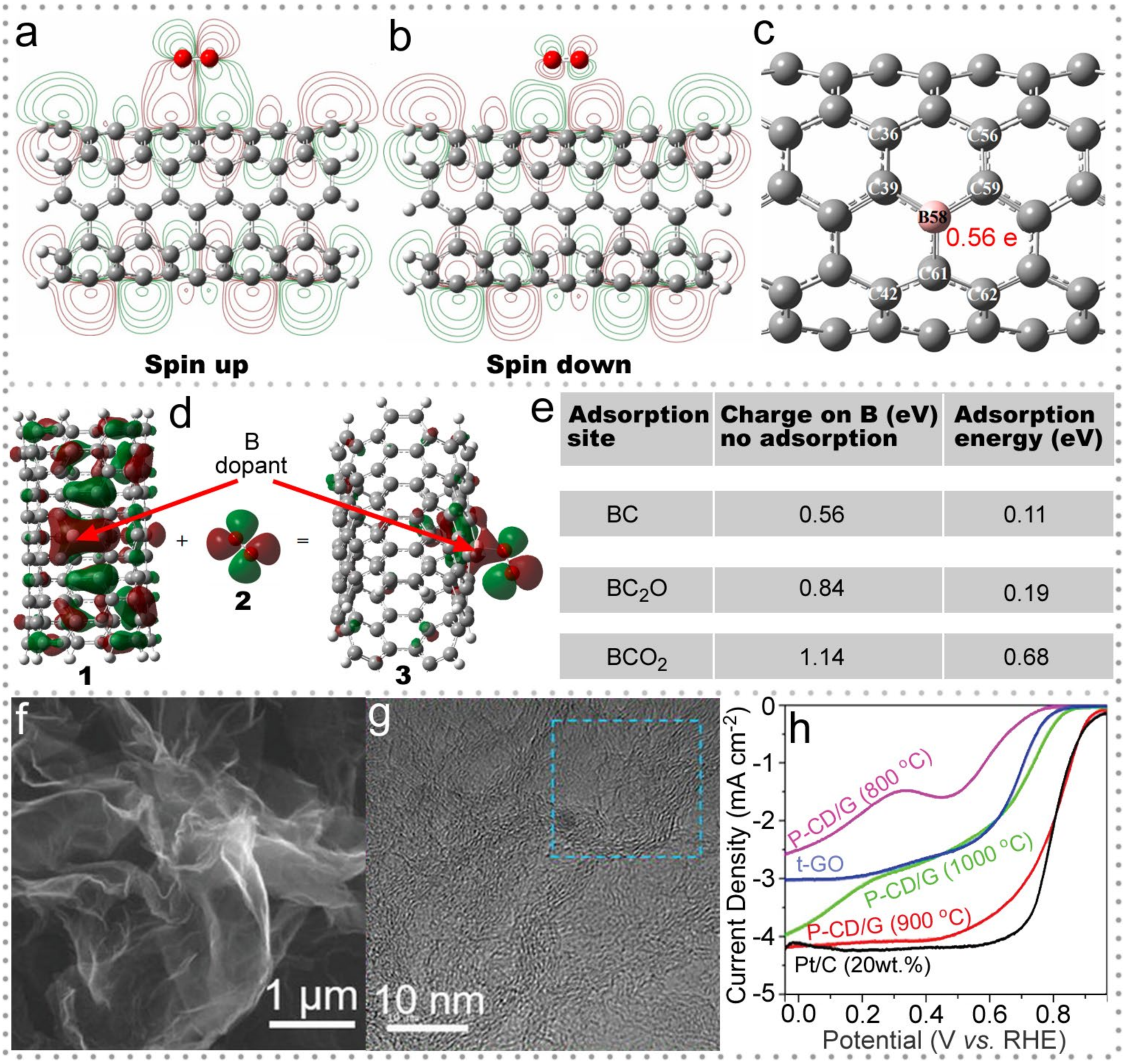

Adsorption site	Charge on B (eV) no adsorption	Adsorption energy (eV)
BC	0.56	0.11
BC_2O	0.84	0.19
BCO_2	1.14	0.68

Figure 3. a) Contour plot for spin up HOMO of physisrobed O_2-CNT (5,5); b) Contour plot for spin down HOMO of physisrobed O_2-CNT (5,5); c) Schematic of CNT (5,5) with substitutional B dopant; d) Schematic of the moecular orbits involved in the O_2 adsorption on B-doped CNT (5,5). 1, 2 and 3 are the spin-down HOMO-1 of B-doped CNT (5,5), LUMO

of the triplet O_2 and spin-down HOMO-2 of O_2 adsorbed on the B-doped CNT (5,5), respectively. (a)-(d) are reproduced with permission.[17] Copyright 2011, John Wiley & Sons; e) Adsorption parameters of BC, BC_2O and BCO_2 sites on CNTs;[17] f-g) SEM (f) and TEM images (g) of P-doped carbon dot/graphene (P-CD/G) sheets; h) Linear sweep voltametry (LSV) curves of various P-CD/G samples obtained at different temperature and the control sample without the P doping (t-GO). The potential was converted using the Nernst equation to be shown versus RHE (pH = 13, 0.2 V of Ag/AgCl reference electrode). (f)-(h) are reproduced with permission.[90] Copyright 2019, John Wiley & Sons.

Hu *et al.* have further evaluated the influence of O element on ORR activation since the B doping treatment was usually accompanied by the incorporation of some O atoms.[17] Their DFT investigation suggested that the charge of B atom and binding strength of O_2 are always improved with both the BC_2O and BCO_2 structures (**Figure 3e**). Nevertheless, compared to N-doped CNTs,[13] the ORR activity of B-doped CNTs is still not good enough.[17]

3.1.3 P and other element dopings

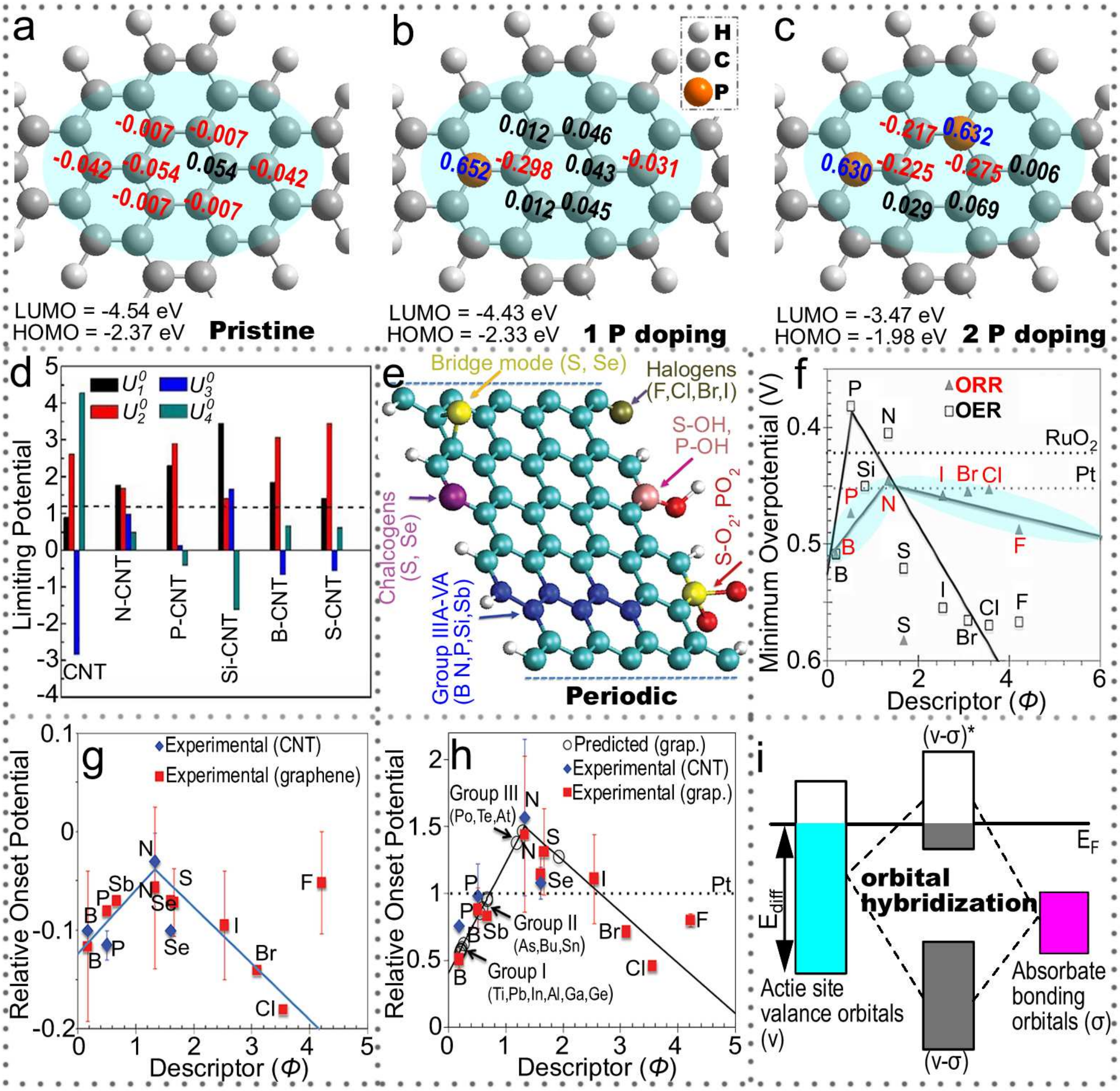

Figure 4. a-c) Net charge of some selected atoms on graphene (a), graphene with one P dopant (b) and graphene with two p dopants (c). Data are retrieved from the reference;[94] d) Limiting potential for associative ORR in acid medium of pristine CNTs and doped CNTs (doped with N, P, Si, B and S). U_1^0, U_2^0, U_3^0, U_4^0 are limiting potentials of reactions of Eqs. 4,5, Eqs. 6,7, Eq. 8 and Eq. 9 at ΔG = 0 (adsorption free energy), respectively. The dashed line corresponds to the equilibrium potential of ORR at 1.23 V. Reproduced with permission.[99] Copyright 2019, IOP Publishing; e) Schematic of the doped graphene,

showing possible doping positions; f) Minimum ORR and OER overpotential versus the descriptor (*Φ*); g) The measured limiting current density normalized by Pt/C electrode current density at 0.5 V (*vs.* saturated calomel electrode/SCE) versus the descriptor; h) The measured relative onset potential as a function of the descriptor. Three groups of dopants are classified in the plot. (f)-(h) are reproduced with permission.[111] Copyright 2015, John Wiley & Sons; i) The orbital hybridization of valence band of active sites and adsorbates bonding orbital. E_F is the highest valence orbital energy of the entire graphene cluster. This figure was prepared according to reference.[113]

The incorporation of the P (electronegativity of 2.19) and S (electronegativity of 2.58) atoms into the carbon structure can also generate interactions between dopants and C atoms, leading to the redistribution of charge and spin density. The activation of carbon materials with P doping for ORR has been well reported experimentally.[20,88-93] For example, Lai *et al.* reported the P doped carbon dots which were loaded on graphene sheets (**Figure 3f**) for ORR.[90] Besides the homogenous P doping, the prepared sample has also various wrinkled surface structure (**Figure 3g**). The undoped sample (t-GO, treated graphene oxide) has suitable ORR activity, which may arise from the edge structure of carbon dots and the wrinkled surface of graphene. The ORR activity can be improved by suitable P-doping (**Figure 3h**). A DFT calculation on similar P doped graphene sheet suggested little positive (0.054 a.u./arbitrary unit) and negative charges (-0.007,-0.042 and -0.054 a.u.) of C atoms in the middle of graphene, which is nearly neutral (**Figure 4a**).[94] In the one and two P doped graphene, the P atoms are charged with 0.652 a.u and 0.630-0.632 a.u., respectively (**Figure 4b-c**). The neighboring carbon atoms of P dopant are negatively charged from −0.217 to −0.275 a.u. (**Figure 4b-c**). It suggested that the P dopant is the active site to adsorb oxygen species, which also improves the charge mobility.[94] Besides, the gap between HOMO and LUMO of graphene is decreased upon the P doping (**Figure 4b-c**), benefiting the electron excitation and electrochemical reaction on the surface. Yang *et al.* used a similar DFT calculation to suggest the ORR reaction species, and that the H_2O, can be bound strongly to the P atom.[95] In the most favorable configuration, O_2 is adsorbed by the P atom via the side-on model and a binding energy of 1.02 eV.[95,96] Such high binding energy makes dissociation of the O-O straightforward, with a relatively low energy barrier (0.38 eV) and large exothermicity (ΔH = 2.07 eV).[95] As predicted, the ORR could take place around the dopant position with a $2e^-$ process to form an OOH intermediate first and then undergo the 4e- reaction to break the O-O bond of OOH.[95] The $4e^-$ process is limited by the reduction of OH to form H_2O with the largest barrier of 0.88 eV, which is similar to that on metal surfaces.[97,98] Compared to P-doped graphene, the P-doped CNTs (8,0) have slightly lower binding energy to O_2 (0.92 eV).[96] This may be explained by the fact that CNTs have surface curvature and need fewer geometrical structure distortions to accommodate the P impurity (in graphene, the P doping drastically changes the geometrical structure, resulting in the protrusion of the P-atom outside the plane).[95-96]

Doping with S atoms can also narrow the energy gap between the HOMO and LUMO of carbon materials.[83] Although the S atom has similar electronegativity (2.58) to that of C (2.55), the large difference in size causes strain and defects in the carbon framework (like that of P doping), which contributes to the ORR activity.[99] Nevertheless, experimental investigations on S-doped carbon materials have not been well explored. Beyond single-element doping with N, B, P and S, other dopants have included Cl, F and Si.[17,32,100-110] We will not discuss these further as their activation mechanism is similar (*e.g.* the change of charge distribution, the distortion of geometric structure, the improved binding strength to O_2 and ORR intermediates).

Table 1. The comparison of carbon materials with and without chemical dopings. In doped CNTs, DFT calculations on the identical model are chosen for comparision. E_b: binding energy, SWNTS: single walled CNTs.

Structures	**Electronegativity**	**E_b to O_2 (eV)**	**Adsorption Model, Mulliken charges (e) on dopant**	**Active Site**	**Ref.**
Graphene	C: 2.55	Planer: 0.007-0.008	No chemical adsorption	NO activity	[51]
	C: 2.55	Zigzag (H terminated): 0.51	Chemical adsorption	C	[51]
	C: 2.55	Armchair: 0.009	No chemical adsorption	NO activity	[51]
CNTs	C: 2.55	SWNTs (8,0), plane: 0.08			[50]
Doped CNTs	N: 3.04	N doped: 0.15	Side-on: -0.718	Neighbouring C	[99]
	B: 2.04	B doped: 0.23	End-on: -0.009	Dopant	[99]
	P: 2.19	P doped: 0.14	End-on: 0.459	Dopant	[99]
	S: 2.58	S doped: 0.73	Side-on: 0.657	Dopant	[99]
	Si: 1.98	Si doped: 1.5	End-on: 0.279	Dopant	[99]

3.1.3 Comparison and combination of different dopings

Next, we directly compare different chemical dopings on the ORR performance. As discussed above, the ORR catalytic activity is highly related to the binding strength of O_2 and

ORR intermediates on the catalyst surface. Activation of the O-O bond needs suitable binding abilities of the active site (**Figures 1g,h**), which are decided by several parameters, such as its electronegativity, charge transfer, geometric structure and electronic distributions. Description and comparison of the ORR activity of different materials using simple and reliable methods is always of interest to the field. **Table 1** compares some parameters of several pristine and doped carbon materials. Among these N-doping creates the highest electronegativity. The charge on the N dopant (-0.718 e) is much higher than that of others, suggesting that N-doped CNTs are likely the best ORR catalyst to activate the O-O bond.[99] The small charge distribution (-0.009 e) suggests that B is not a good candidate to promote ORR, which contradicts with the result reported by Hu *et al.* by showing large charges on the B and good ORR performance (**Figure 3d,e**).[17] In B-doped CNTs, the ORR activity may have also been promoted by the O species (**Figure 3e**). Wang *et al.* compared the limiting potential of four key dissociative ORR reactions (Eqs. 4,5/step 1, Eqs. 6,7/step 2, Eq. 8/step 3 and Eq. 9/step 4) of different CNTs in acidic media (pH = 0, **Figure 4d**).[99] In CNTs doped with N, B, P, S or Si, the step 2 reaction (Eqs. 6 and 7) is favored, with the limiting potential larger than the equilibrium potential of 4 e^- ORR in an acidic medium (1.23 V, **Figure 4d**). Step 4 (Eq. 9) is the rate-limiting reaction in N-, P- and Si-doped CNTs, while step 3 (Eq. 8) is the rate-limiting reaction of pristine, B-, and S-doped CNTs. Among all these CNTs, the N-doped CNTs give the highest limiting potentials for all four dissociative reaction steps (**Figure 4d**).

Xia *et al.* provided a more compensative comparison of the ORR activity of different doped carbon nanomaterials (possible doped structures are shown in **Figure 4e**).[111] They introduced the descriptor of $\Phi = (E_X/E_C) \times (A_X/A_C)$, to describe the effect of a dopant on electron transfer and reaction energy in both ORR and oxygen evolution reaction (OER). E_X and E_C represent the electronegativity of the dopant (X) and carbon (C), respectively. The electron affinity (A) of X and C represents the energy released when a neutral atom gains an extra electron to form a negatively charged ion in the chemical reaction. This descriptor has an intrinsic relationship with the intermediate adsorption which decides catalytic activities. When Φ ranges from 1 to 3, the ORR activities of regulated carbon materials could exceed that of Pt (**Figure 4f-h**). With this descriptor, N was identified as the best dopant to activate the ORR of carbon materials (**Figure 4f-h**). This descriptor has also been used to predict the catalytic activity of various other doped carbon materials. **Figure 3h** shows such indicator, where three groups of dopants are classified. Group I includes Ti, Pb, In, Al, Ga and Ge and are similar to B dopants. Group II (As, Bi and Sn) and III (Po, Te and At) are close to the O and N dopants, respectively.[111]

Inspired by the *d*-band center theory of metal catalysts,[112] Qiao *et al.* also proposed a method to establish the correlation between the binding strength and molecular valence orbital levels of each ORR active atoms, to describe the ORR activity of carbon materials (**Figure 4i,** the analyses was based on graphene materials).[113] The adsorption energy of ORR intermediates (*e.g.,* OH*) is directly affected by the valence orbital of the active center that participates in the bond formation. The adsorption energy of O_2 and ORR intermediates has a nearly linear relationship with E_{diff}, defined as the gap between lowest valence orbital of the active site and highest valence orbital energy of the entire graphene cluster (Fermi energy level in the form of natural atomic orbitals, **Figure 4i**). The adsorption energy is raised from the hybridization of valence band (v) of active site and bonding (σ) orbital of adsorbed species, to form bonding (v-σ) and antibonding (v-σ)* states. The filling of the antibonding state decreases the binding strength between active sites and adsorbates, which is induced by a lower valence band of active site.[113] Therefore, to improve the binding ability to the ORR intermediates, the active sites should possess a higher valence orbital energy. Such simplification of the relationship between binding ability and orbital hybridization model (**Figure 4i**) will be highly useful in discussing geometric effects (**Section 3.2**). With these principles, Qiao *et al.* plotted the ORR activity with different dopants, which are consistent with the results obtained with the descriptor Φ.[111,113] It should be noted that all the above descriptors are mainly based on the 4e$^-$ dissociative process, while the 2e$^-$ associative process may not need such a high degree of O-O bond activation.

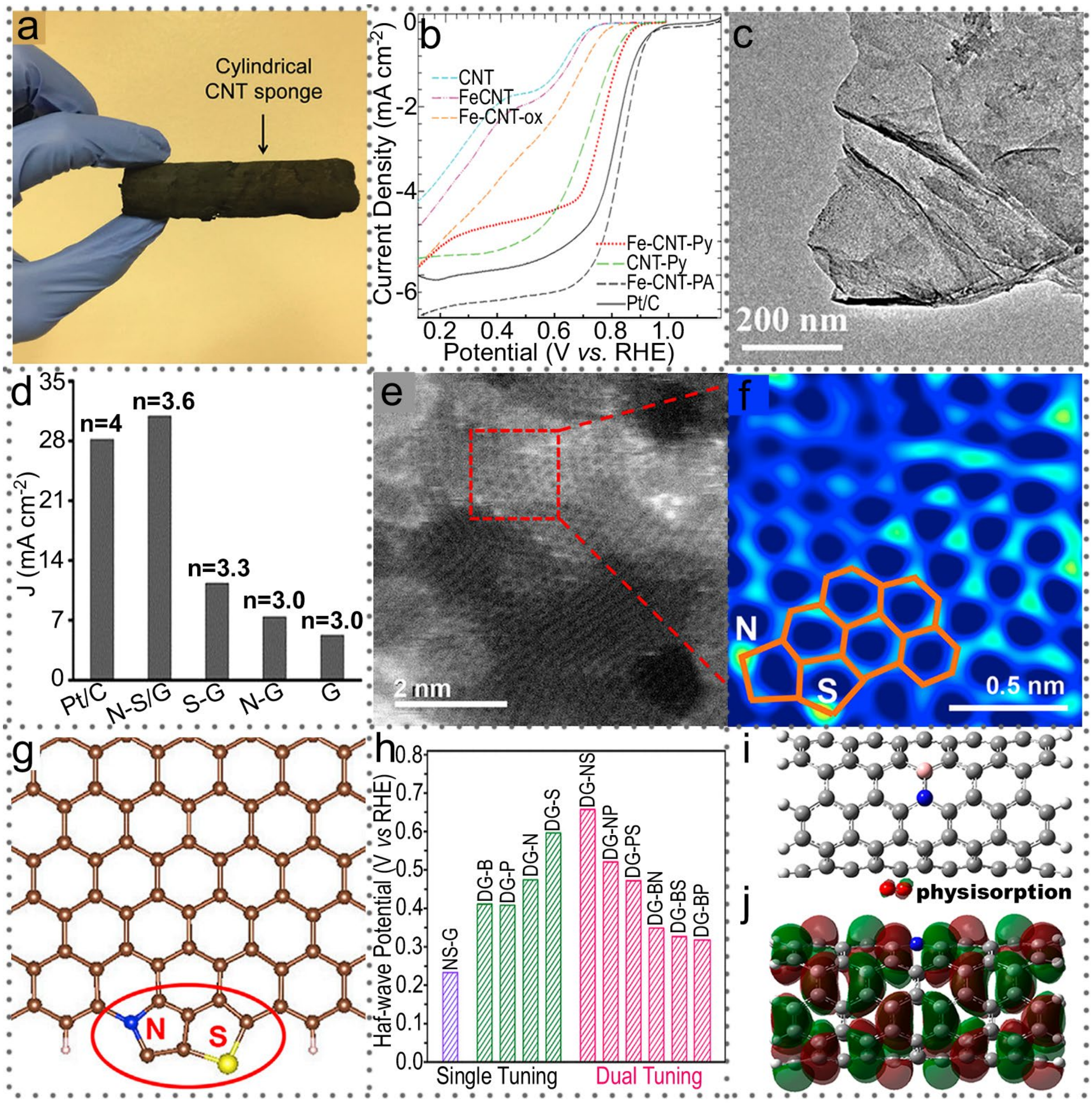

Figure 5. a) Photograph of a CNT sponge; b) Linear sweep voltammetry (LSV) of various catalysts in O$_2$-saturated 0.1M KOH electrolyte. PA and Py mean polyaniline and polyaniline, respectively. The potential was converted using the Nernst equation to be versus RHE (pH = 13, 0.2 V of Ag/AgCl reference electrode); (a)-(b) are reproduced with permission.[116] Copyright 2015, Royal Society of Chemistry; c) Transmission electron micrograph (TEM) image of doped graphene sheets; d) Limiting current of different samples and the corresponding electro-transfer number (at -0.6 V *vs.* Ag/AgCl). (c)-(d) are reproduced with permission.[114] Copyright 2012, John Wiley & Sons; e,f) High-angle annular dark-field (HAADF) scanning TEM (STEM) image of the defected graphene sheet with N and S dopants (DG-NS) (e) and corresponding fast Fourier transformation-filtered image (f); g) Schematic structure of the DG-NS; h) Half-wave potential comparison of different samples (in O$_2$ saturated 0.1M HClO$_4$). DG: defected graphene. NS-G: N and S dual doped graphene. The suffixes show the dopant elements. (e)-(h) are reproduced with permission.[119] Copyright 2020, Cell Press; i,j) Bonded B and N co-doped CNTs (5,5) (i) and corresponding HOMO plot of the O$_2$ adsorption configuration (isodensity value of 0.007 au.). N, B, C and O atoms are represented with blue, pink, dark gray, light gray and red color, respectively. (i)-(j) are reproduced with permission.[80] Copyright 2014, American Chemical Society.

Beside the above discussed single doping, several multiple doping strategies of carbon materials have been reported, aiming to further regulate the ORR activity.[80,114-118] For example, Yu *et al.* reported the fabrication of a CNT sponge (**Figure 5a**) catalyst with optimum C-N-Fe coordination, which showed stronger catalytic performance than a Pt/C catalyst in O_2 saturated 0.1 M KOH (**Figure 5b**).[116] Compared to CNT, FeCNT (CNTs contain Fe) and Fe-CNT-ox (Fe-CNT annealed in air), the materials CNT-Py (CNT with N doping, pyridine), Fe-CNT-Py (Fe-CNT with N doping, pyridine) and Fe-CNT-PA (Fe-CNT with N doping, polyaniline) showed significantly improved ORR activity. Although the detailed functions of the Fe and N are not clear, this report suggested that the formation of nitrogen-iron coordination could provide greater ORR activity than N-doping alone. Qiao *et al.* also reported S and N dual-doped graphene sheets (**Figure 5c**) for ORR.[114] Comparison of different samples suggested that the dual doping offered much higher limiting current density than that of either S- or N-doped graphene alone (**Figure 5d**). Besides, the ORR of the S and N dual-doped graphene has a higher electron transfer number than single (S or N) doped material, which is beneficial to fuel cells applications. Based on DFT calculations, Qiao *et al.* suggested that the S and N doping generate "synergistic effects", in which electron spin and charge densities are redistributed to create more active carbon atoms surrounding the dopants.[114] However, the DFT calculations reported by Shao *et al.* gave a different viewpoint of S and N doping not having obvious "synergistic effects" that benefit the ORR.[117] Instead, the improved ORR performance was believed to arise from pre-treatment S doping resulting in the formation of additional pyridinic N-structures. Otherwise, the ORR activity would be decreased if the pre-formed pyridinic N structures are disrupted by S doping.[117] Yao *et al.* also suggested that the dual doping of graphene has no significant uplift of the ORR (**Figure 5e-h**)[119] and, in particular, N and S dual-doped graphene materials have very poor ORR activity (**Figure 5h**). They fabricated defected graphene sheets with pentagon C5 structures (**Figure 5e-g**) and systematically compared the ORR effects on various single and dual doping treatments (**Figure 5h**). Both the DFT and experimental investigations indicated that the heteroatoms generally had a limited contributed to the ORR, although the ORR promotion is significant if these dopants are at certain defected structures (*e.g.* the C5 structure).[117]

Again, a research reported by Hu *et al.* suggested that B and N dual-doping cannot activate CNTs for ORR (with only physisorption to O_2, **Figures 5i-j**), if the B and N are bonded to each other.[80] The improvements can only happen if B and N are separately doped into the carbon structure without the predicted "synergistic effects" (B and N doping improve the catalysis separately).[80] The above controversy seems to have arisen from an evolving understanding of the more complex role of structural defects on the ORR than might initially be expected.

3.2. Defects

All the above discussion suggests that defects in carbon materials are critical to determining ORR activity and selectivity, which has been overlooked in many early studies. Now, we start to discuss how these defects can be used to improve the ORR.

3.2.1 Edge and Pentagon Structures

As discussed above (**Section 3.1.1**), the zigzag edge has very high ORR activity (**Figure 2i**). Recent experiments on edge-enriched graphene and CNTs also confirmed their high catalytic activity.[26,120-122] In 2018, Shui *et al.* reported the ORR on partially-unzipped CNTs and their application in fuel cells (**Figure 6a-b**).[26] They initially unzipped CNTs to give edge structures and then performed annealing to remove surface O-containing groups from samples. s the control sample, partially- and fully-unzipped CNTs either undoped or N-doped were prepared and measured. Both the pristine and N-doped partially-unzipped CNTs exhibited better ORR activity than doped/undoped fully-unzipped CNTs. The co-existence of CNTs and unzipped nanoribbons (**Figure 6a**) in the partially-unzipped sample was considered to benefit the electrochemical dynamics.[26] In alkaline media, partially-unzipped CNTs exhibited a half-wave potential of 0.819 V, which is close to that of Pt/C (0.84V) and N-doped control samples (0.839 V).[26] In acidic media, the onset and half-wave potentials of partially-unzipped CNTs were measured as 0.76 and 0.633V, respectively, which were higher than those of the N-doped control sample. Shui *et al.* then suggested that the lower ORR activity of

N-doped control samples in acidic media is due to proton adsorption, which weakens a CNT's ability to bind O_2 and ORR intermediates.[26,123,124] This mechanism is also relevant in pure zigzag structures, where protonation is also common in acidic media.[47,125-127] In both acidic and alkaline media, the number of electrons transferred in the ORR with partially-unzipped CNTs is measured to be 3.6 – 3.9 through a direct $4e^-$ dissociative process (**Equations 1-3**), which is close to that found using plasma-treated graphene sheets (3.85).[120] It should be noted that the catalytic activity and selectivity may be different with unzipped CNTs (nanoribbons) and CNTs due to their different C-C/C=C bond lengths (longer bond length means stronger binding of O_2).[70]

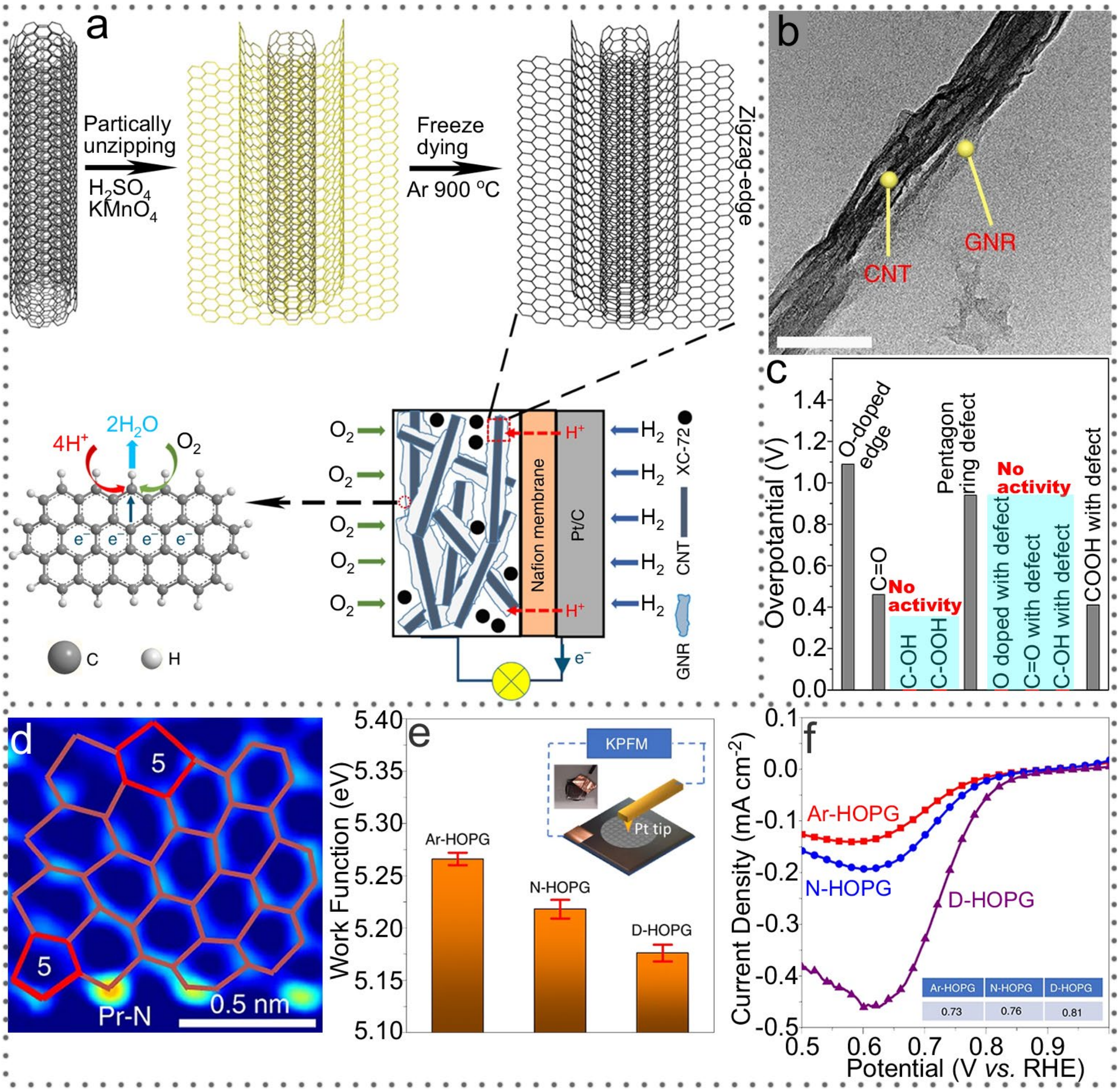

Figure 6. a) Schematic of the unzipping of CNTs and their application in fuel cells; b) Transmission electron micrograph (TEM) of partially-umzipped CNT. Scale bar: 100 nm; (a),(b) are reproduced with permission.[26] Copyright 2018, Springer Nature; c) ORR overpotential of different edge structures. Data are retrieved from the reference;[122] d) Fast Fourier

transformation-filtered image transferred from the HRTEM image; e) The local work function of the edge areas of Ar-HOPG, N-HOPG and D-HOPG. The inset is the scheme of the KPFM measurements; f) LSV curves of Ar-HOPG (red), N-HOPG (blue) and D-HOPG (purple) in 0.1 M H_2SO_4 solution. Inset table shows the correlated potential (V, *vs.* RHE) at 0.05 mA cm^{-2}. (d)-(f) are reproduced with permission.[129] Copyright 2019, Springer Nature.

Shui *et al.* performed further DFT calculations to support the high activity of zigzag-edge carbon atoms, and suggested that O doping of carbon-structure edges would reduce their catalytic activity.[26] However, a DFT calculation reported by Want *et al.* indicated that some O-containing groups can actually improve the ORR activity of neighboring C atoms because of the charge redistribution induced by oxygen.[122] In their DFT calculations, the overpotential of different armchair and zigzag edges were compared, where they were either O-doped, C=O terminated, C-OH terminated, C-OOH terminated and/or contained pentagon defects (**Figure 6c**). Of these, the pentagon-defected structure with C-OOH species had the lowest ORR overpotential. The defect-free structure with C=O edge-termination also had low ORR overpotential, and lower than the pure edge structures (**Figure 6c** and **Figure 2h**). Other structures such as zigzag edges with C-OH and COOH termination, and pentagon-defected structure with O dopant and C=O/C-OH termination have proved to be ORR inactive.[122]

Compared to the hexagonal zigzag edge, the pentagonal edge (**Figure 6d**) has much higher catalytic activity for the ORR, although this structure is not common in highly-crystallized graphite.[119,128-131] In 2018, Mu *et al.* used DFT calculations to compare ORR activity on hexagonal C6 and pentagonal C5 carbon atoms.[131] Unlike the C6 structure, the C5 structure shows a narrowed HOMO-LUMO band structure and has a larger change density gap and much higher adsorption energy to O_2, all of which enhances the catalytic activity of C5 carbons, including those at edges, over C6 carbons.[131] Experimentally, Yao *et al.* prepared defected pentagonal carbon (see **Figure 6d**, D-HOPG) and pyridinic N-doped HOPG (N-HOPG).[131] The D-HOPG was fabricated by first doping N into the edges of HOPG at 700°C and then removing it at 1150 °C. Kelvin probe force microscopy (KPFM) was used to measure the electron-donating capability of edge areas of Ar-HOPG (Ar annealed), N-HOPG and D-HOPG. D-HOPG had the lowest local work function at edges (5.18 eV), corresponding to the highest electron-donating capability.[131] Further LSV scan confirmed the best ORR catalytic activity of the D-HOPG edge structure (**Figure 6f**).

All the above investigations suggested that the edge structure of carbon materials is critical to their use as catalysts in the ORR. In particular, introduction of pentagonal defects has proven particularly effective at improving catalytic activity.

3.2.2 Wrinkles and Corrugations

Besides the zigzag and pentagonal edges, topological defects such as wrinkles, corrugations (ripples) and structure dislocations (strain) also affect the adsorption ability of carbon materials to O_2. In electrochemical energy storage, the corrugation and strained structures of 2D materials have been shown to enhance chemical activity, binding strength and the solvent-accessible surface area.[47,132-137] These structural asymmetries give the improved binding ability through the local polarization of electronic states and a higher DOS around the Fermi level, which means that local chemical potential is enhanced at curvatures.[47,138,139] Similar phenomena have been observed in 2D MoS_2 sheets when a tensile strain is used to introduce electronic states close to the Fermi level.[44,45,140-143] Combing the above orbital hybridization description model (**Figure 4i**), the formation of these in-gap electronic states in carbon materials could, in principle, lift the valence orbital energy level, reducing the antibonding state and increasing the binding strength to adsorbates.

Corrugation of graphene (**Figure 7a**) is extremely common due to anisotropic strain relaxation.[144-146] Understanding of the binding ability of local corrugations can be gained by using DFT calculations to consider 'waved' graphene, which has a periodic ripple structure and significantly different electronic and magnetic properties compared with flat graphene.[133,139,144,145] **Figures 7b,c** show the calculated pyramidalization ("π-orbital axis vector"/POVA, will be further introduced in **Section 3.2.4**) angles of carbon atom positions within one wavelength of waved graphene under 10-50% compression with the ripples along the armchair and zigzag directions.[139] The compression (ε) is defined as the value of (C_0-

C)/C_0, where the C_0 and C are the starting and compressed wavelength, respectively. The graphene is more wrinkled with higher compression (**Figures 7b,c**). The bending at the bridge between two hexagons decouples the big π bonding states in neighbouring hexagons and generates charge redistribution.[139] DFT calculations suggested that the O_2 molecules can be chemically adsorbed with only the side-on model at the rooftop ripple position (has the highest chemical activity) of waved graphene.[133] The C-O bond length decreases, and the O-O bond length increases with the increase of compression (**Figure 7d**). In ziagzag graphene nanoribbons with an oxygen atom bonded to C edges, bond lengths of C-O and O-O are 1.65 and 1.30 Å, respectively (compared to a bond length of 1.22 Å in isolated free O_2 molecules).[51] In O_2-chemically-adsorbed waved graphene (**Figure 7d**), the bond length of C-O becomes < 1.46 Å, while the bond length of O-O is close to 1.52 Å upon 50% compression.[133] In this case, the C-C bond also increases to 1.721 Å. These values may be different in practice, but the calculated trends suggest that O_2 adsorption on waved graphene is strong enough for the O-O bond activation. In flat graphene (ε = 0), chemical adsorption is difficult and endothermic, having a chemical adsorption energy of 0.95 eV. The chemical adsorption of O_2 becomes exothermic at ε = 30% and the adsorption energy decreases to -0.62 eV at ε = 50% (**Figure 7e**).[133] The O_2 binding of highly compressed, waved graphene is stronger even than that of zigzag-edge C atoms (end-on adsorption, **Table 1**). Besides, compared to the end-on adsorption at the edge, the side-on adsorption of O_2 on waved graphene suggests that the O-O bond is more likely to be dissociated to benefit the $4e^-$ ORR process. The DFT calculations reported by Tozzini *et al.* also suggest that tensile strain results in stretched C-C/C=C bonds but compressive strain results in a limited reduction of the C-C/C=C bond length, with sites tending to pyramidalize instead, resulting in higher surface activity and binding ability, and a transformation of sp^2 orbitals to unpaired sp^3.[147]

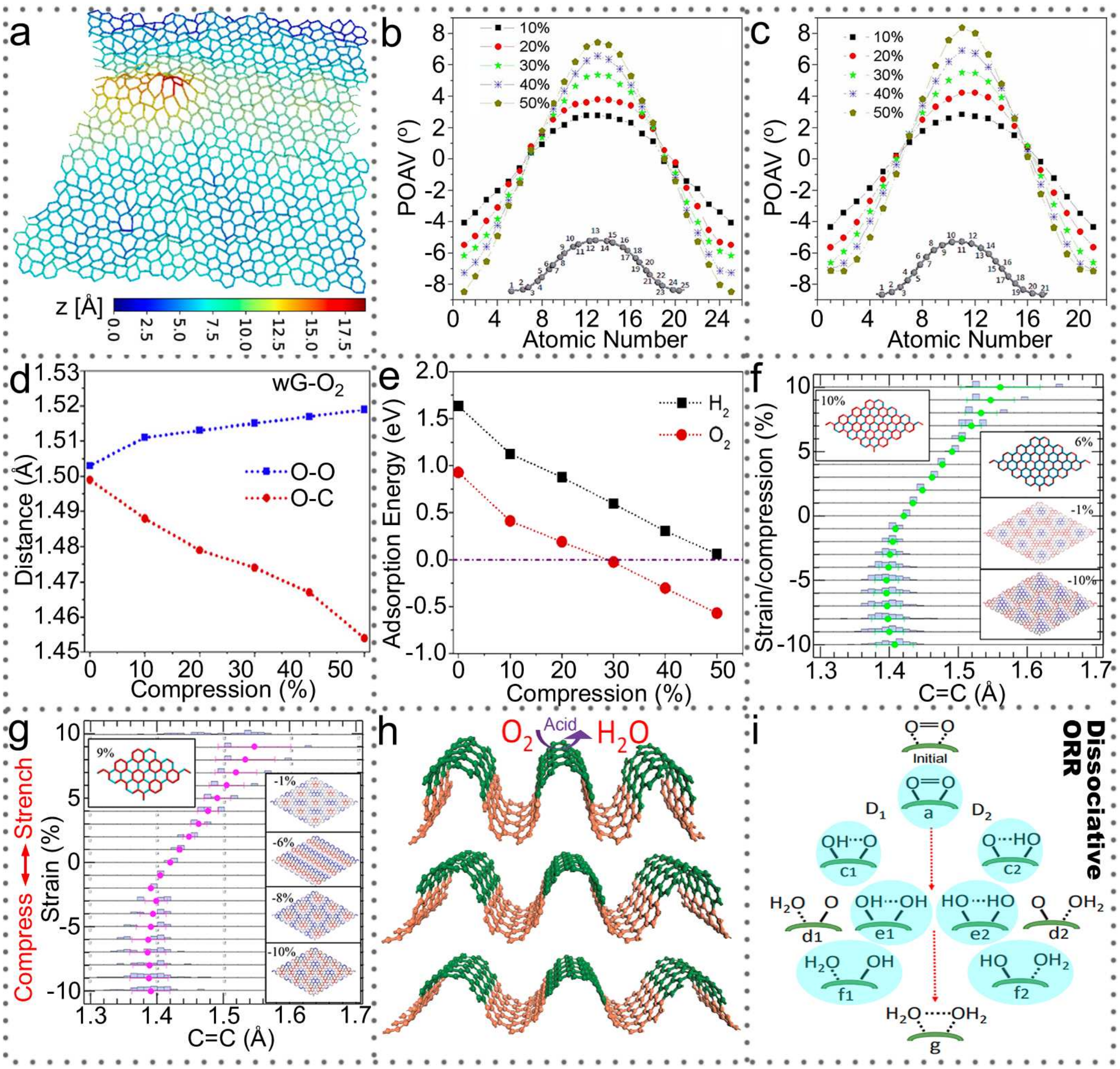

Figure 7. a) Perspective view of a graphene structure showing surface corrugation. The z position out of plane is color coded. Reproduced with permission.[146] Copyright, 2018, IOP Publishing; b,c) DFT-calculated pyramidalization angles within one wavelength of waved graphene with ripples along armchair (b) and zigzag directions (c). Reproduced with permission.[139] Copyright 2014, Springer Nature; d) DFT-calculated adsorption distance between waved graphene and O_2 molecule. wG-O_2 means waved graphene bound to O_2; e) DFT-calculated adsorption energies of H_2 and O_2 on waved graphene as a function of compression. (d)-(e) are reproduced with permission.[133] Copyright 2017, Elsevier; f-g) The C-C/C=C distance distribution at different cell strain with 4√3×4√3R30 (e) and 3√3×3√3R30 cells (f). The inset shows the selected strained and contracted structures. In the contracted structures, the blue and red colors represent the up and down displacement in the z direction (out of plane). Reproduced with permission.[147] Copyright 2015, American Chemical Society; h) A proposed model of waved graphene for ORR (C atoms displayed in two different colors); i) The proposed ORR pathways (highlighted) of the waved graphene. (h),(i) are reproduced with permission.[148] Copyright 2017, Springer Nature.

In 2017, Pan *et al.* reported DFT calculations of the ORR on waved graphene.[148] The adsorption energy of O_2 at the top of ripple position was calculated as to be -0.09, -0.36 and -0.62 eV under compressions of 30%, 40% and 50%, respectively, the latter two of which being larger than the O_2 adsorption energy on N-doped graphene (-0.20 eV).[148,149] Upon N-doping waved graphene, O_2 adsorption energy with 30%, 40% and 50% compression changed to -0.83, -1.05 and -1.22 eV, respectively, suggesting improved binding abilities.[148] All of these cases are also marked by significant charge transfer from the waved graphene to the O_2 molecule, sometimes as close to one electron. On waved graphene with compression of 50% and in acidic media, the adsorbed O_2 undergoes a sequence of: O-O bond activation; formation of OH---O (or O---OH, c1 and c2 in **Figure 7i**); formation of OH---OH (or HO---HO, e1 and e2 in **Figure 7i**); and, finally, formation of H_2O (f1, f2 and g in **Figure 7i**). Any H_2O_2 decomposes into OH---OH (e1 and e2 in **Figure 7i**, easily dissociate), suggesting that the dissociative $4e^-$ mechanism is the mostly likely ORR pathway.[148] Therefore, carbon materials can be activated for ORR by forming local wrinkles, corrugations and ripple structures in their surface. It should be noted that with these modifications, the improved binding ability to O_2 is comparable with or stronger than that of flat N-doped carbon materials (see **Table 1**).

3.2.3 Point Defect and Lattice Dislocation

Defects such as point defects and lattice dislocations are also universal in carbon materials.[150-156] The structural asymmetry and strain induced by these defects create significant local charge redistribution, which will affect the ORR activity.

Since carbon atoms have several possible electron orbital hybridizations, the graphene lattice has the ability to reconstruct by forming non-hexagonal rings (**Figure 8a**). The formation of a C vacancy causes distortion of nearby C rings and creates dangling bonds towards the vacancy site. This increases the local DOS (LDOS) at the Fermi energy, which is spatially localized at the dangling bonds.[151] This phenomenon has been experimentally confirmed by Brihuega *et al.*[152] They created the single C vacancy on HOPG and measured the vacancy position with scanning tunneling microscopy (STM) and scanning tunneling spectroscopy (STS). The dangling bond gave a protrusion around the vacancy position in the STM image (**Figure 8b**) while STS measurement confirmed the significantly increased LDOS at around the Fermi energy level (**Figure 8c**).[152] A pentagon ring reconstruction is one such point defect and shows very high catalytic activity on the ORR, as we mentioned above.[119]

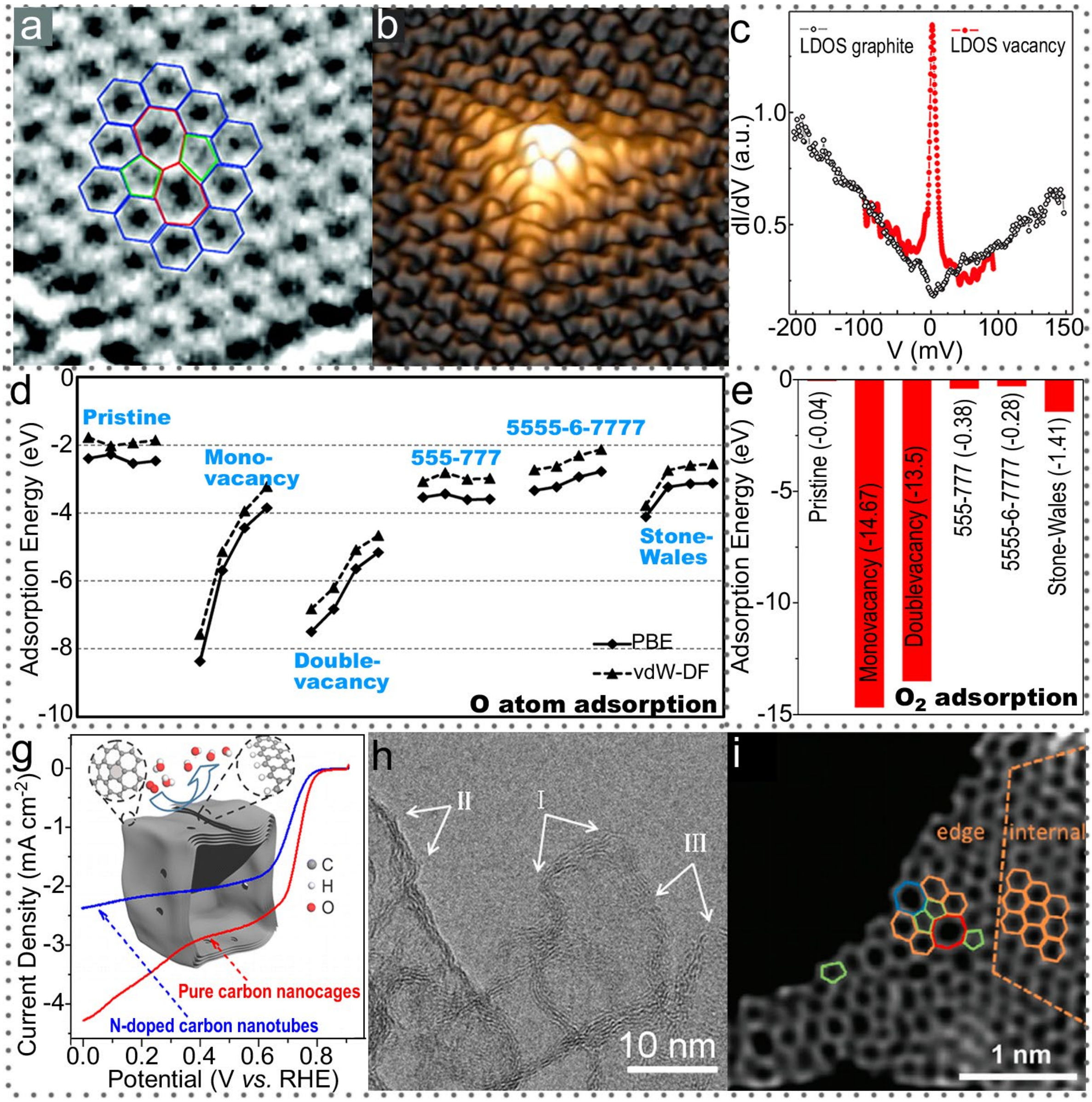

Figure 8. a) HRTEM image of the reconstructed vacancy of graphene lattice. Reproduced with permission.[150] Copyright 2008, American Chemical Society; b) 3D scanning tunneling microscopy (STM) image of a single isolated C vacancy on HOPG; c) Scanning tunneling spectroscopy (STS) measurement of pristine HOPG without vacancies (black dotted line) and HOPG with a single vacancy (red dotted line, measured on the top of the vacancy). Reproduced with permission.[152] Copyright 2010, American Physical Society; d) Calculated O adsorption energies using Perdew-Burke-Ernzerhof (PBE) without (solid line) and with a vdW-DF correction (dashed line, van der Waals correction). For each defect, the data points from left to right correspond to the coverage of 1 to 4 O atoms. Reproduced with permission.[157] Copyright 2013, American Chemical Society; e) Comparison of O_2 adsorption on the basal surface of graphene and different defect sites. Data are retrieved from the reference;[157] g) Schematic of the defected carbon nanocage, and the ORR LSV comparison with N-doped CNTs in 0.1 M KOH. The potential was converted with Nernst equation to versus RHE (pH = 13); h) Transmission electron microscope (TEM) image of a carbon nanocage; (g),(h) are reproduced with permission.[23] Copyright 2015, American Chemical Society; i) HAADF STEM image of the defected graphene with reconstructed ring structures. Reproduced with permission.[163] Copyright 2016, John Wiley & Sons.

The formation of the multiple-C vacancies may lead to more complex defect configurations, such as boundaries, pores and lattice dislocations. Broadly, as with single C vacancies, electronic redistribution and dangling bonds also exist around multiple-C vacancies if the various reconstructed structures around the defect site cannot match to each other (e.g., the combination of hexagonal and non-hexagonal structures).[151] As discussed above, the binding ability to O_2 in these defect sites is generally enhanced from the pristine graphene lattice. Pachter *et al.* used DFT calculations to evaluate the adsorption of O and O_2 on different defect sites,[157] including the mono-vacancy, double-vacancy, 555-777 (divacancy, containing three pentagonal and three heptagonal cells),[158] 5555-6-7777 (containing three pentagonal, one hexagonal and three heptagonal cells)[159] and Stone-Wales defects (no C vacancy, pure reconstruction of a graphenic lattice between pentagons, hexagons and heptagons). They suggested that these representative defects have very high adsorption energies for O atoms (**Figure 7d**) and O_2 molecules (**Figure 7e**). O_2 directly dissociates at the mono and double-vacancy positions, with adsorption energies of -14.67 and -13.5 eV, respectively.[157] In the other defect positions, the adsorption energy of O_2 also decreases significantly from -0.04 eV of pristine graphene to -0.38 (555-777), -0.28 (5555-6-7777) and -1.41 eV (Stone-Wales).[157] Such adsorption energies are comparable to or better than that of chemically-doped carbon materials (**Table 1**), suggesting the likely high ORR catalytic activity of these reconstructed structures. A DFT calculation reported by Xia *et al.* also indicated that various reconstructed defect structures at both edge and boundary positions are highly active for ORR, and facilitate the $4e^-$ process.[160]

The lattice dislocation in many activated carbon materials can be considered as the assembly of various point defects, wrinkles and corrugations. Several defect-containing carbon materials have been proposed for the electrochemical ORR.[23-25,161-165] For example, Hu *et al.* reported the ORR on defected carbon nanocages, which had higher catalytic activity over that of N-doped CNTs (**Figure 7g**).[23] Unlike the N-doped CNTs, the LSV of the defected carbon nanocage has two reaction stages, which may correspond to the $2e^-$ and $4e^-$ processes. The electron transfer number in the defined potential range (**Figure 8g**) was calculated as around 2.9.[23] These carbon nanocages have clear lattice dislocations and defected structures (**Figure 8h**). Based on DFT modeling, Hu *et al.* concluded that various defected structures (*e.g.,* pentagons and zigzags) were the main contributors to the ORR activity.[23] Yao *et al.* also confirmed that the reconstructed ring structures of graphene materials (**Figure 8i**) could improve the ORR activity.[163] As we discussed above, topological defects such as wrinkles and corrugations in many highly-activated carbon materials are likely to catalyze the ORR strongly but this has been discussed only rarely. The above discussion suggests that these defected structures are highly active for ORR and facilitate the 4e$^-$ process. Nevertheless, the measured electrocatalytic activity and ORR electron transfer number of most defected carbon materials are still much lower than that of the N-doped CNTs (electron transfer number close to 4).[13,23-25,161-163] Significant efforts are still neeYded to enrich and purify these defected structures, enabling highly efficient and selective ORR.

3.2.4 Surface Curvature of CNTs

Our above discussions imply that the surface of pristine CNTs cannot chemically adsorb O_2 (see **Table 1**). However, the curvature of CNTs and similar BN nanotubes have been suggested to be highly important to improve gas and chemical adsorptions.[164,165] The surface curvature of CNTs has similarities to the corrugated structure and associated strain of graphene layers, and may be critical in affecting the chemical affinity for O_2 and thus to increase the catalytic activity. In CNTs, it makes the carbon atoms acquire sp^3-like properties that weaken the binding of carbon atoms. Various studies indicated the link between surface curvature and its associated ability to bind external molecules.[103,166-174] However, the precise role curvature plays in regulating the adsorption of O_2 and ORR intermediates is still under debate.

Early in 2000, Zettl *et al.* reported the sensitivity of electrical resistance and thermoelectric power (**Figure 9a**) of SWCNTs to exposure to O_2.[173] The electrical response was reversibly altered by O_2, which suggests that SWCNTs can chemically interact with O_2 with significant charge transfer resulting. Such interactions can also be induced by defect structures. Ajayan *et al.* also found that multi-walled CNTs (MWCNTs) can chemically interact with O_2 to enable

ORR.[174] Nevertheless, their DFT calculations on SWCNTs (3,3) suggested that curvature plays only a small role in O_2 adsorption and charge transfer. By contrast, the curvature is responsible for the improved ORR activity of tip caps and defect sites (*e.g.* pentagonal sites, pentagon-heptagon junctions) of CNTs.[174] Monreno *et al.* have also investigated the effect of local curvature on the adsorption of O_2 on SWCNTs.[172] For armchair CNTs, the local curvature radius (R') is equal to the tube radius (R). In zigzag CNTs, R' is larger than R due to the ellipsoidal shape of the cross-section along C-C bonds (**Figure 9b**).[172,175] (3,3)/metallic, (5,0)/semiconducting, (5,5)/metallic and (8,0)/semiconducting SWCNTs were chosen for the comparison, which have a curvature radius (R') of 2.04, 2.32, 3.39 and 3.71 Å, respectively. They found that the O atoms can be strongly chemisorbed on the bridge site (between the C-C bonds) of CNTs, and the adsorption energy is increased with the curvature. O_2 molecules can only be physisorbed on the surface of CNTs with large distance between the O_2 and a bridge site (~3 Å, interaction mainly from van der Waals forces), which also increased with the curvature.

DFT calculations reported by Liu and Radovic *et al.* indicated that the chemical interaction between O_2 and CNTs is possible, while the adsorption energy decreases with increasing tube diameter, i.e. a weaker interaction is seen as the curvature decreases.[171,176] The surface of metallic CNTs is more reactive than that of semiconducting CNTs. Recently, Yang *et al.* investigated ORR activity with CNTs.[166] They proposed a localized geometric descriptor of CNTs based on the pyramidalization angle to report ORR activity. This angle directly reflects the local curvature of a surface and the torsion of the π orbital system (**Figure 9c**). In POAV (π orbital axis vector) analysis,[177-178] the POAV is chosen in the z-direction (local surface normal) and has angles ($\theta_{\sigma\pi}$) equal to the σ orbitals of C_0C_1, C_0C_2 and C_0C_3 (**Figure 9c**). The "pyramidalization angle" (θ_p) was defined as ($\theta_{\sigma\pi} - 90^o$).[166] Yang's DFT calculations suggested that the adsorption free energy of pristine CNTs, and B- and N-doped CNTs are all highly correlated with the pyramidalization angle, which all increased with the surface curvature (**Figure 9d**). A volcano plot implies that low overpotentials of 4e$^-$ ORR can only be reached using highly-curved CNTs (**Figure 9f**), which are unstable and difficult to fabricate. Nevertheless, high activity of weakly-curved CNTs can be obtained with suitable chemical doping.[166] By combining the above approaches with defects, it might be possible to achieve highly-active ORR reaction on weakly curved and defected CNTs (*e.g.* with lattice distortions, edge structure, and point defects of MWCNTs).

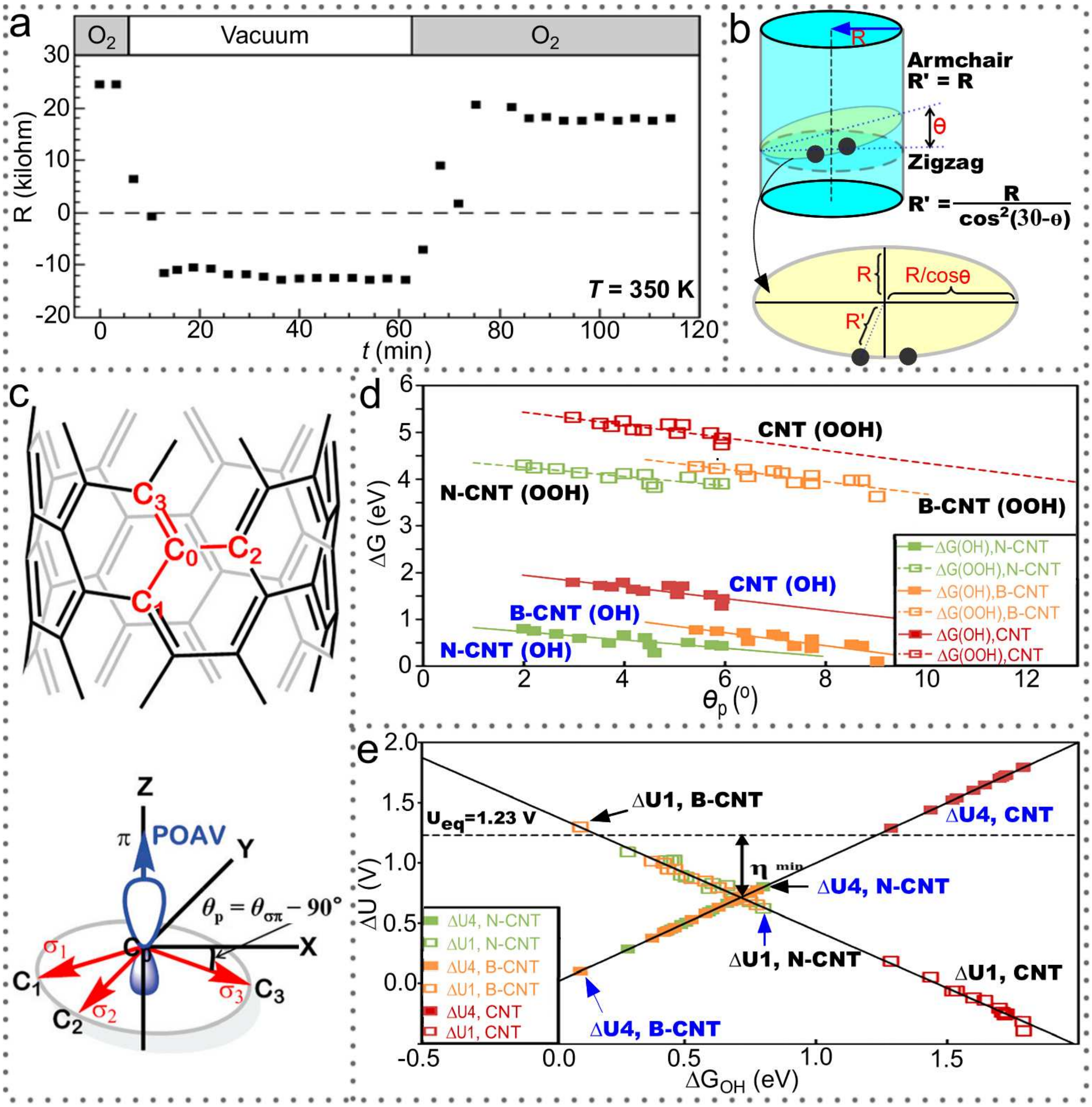

Figure 9. a) Sensitivity to environmental conditions of thermoelectric power S for SWNTs at 350 K. Reproduced with permission.[173] Copyright 2000, AAAS; b) Schematic of the cross-section of a CNT with radius R and local curvature radius of R' along the C-C bond inclined by angle θ. This figure is prepared according to reference.[172] c) Schematic of the pyramidalization angle (θ_p) on pure CNTs. C_0 is the active C atom, surrounded by the C_1, C_2 and C_3 C atoms. For B- and N-doped CNTs, one of the above C atoms may be replaced by B or N; d) Plots of adsorption free energies of OH (solid line) and OOH (dashed line) against the pyramidalization angle; e) Adsorption free energy of OH as the descriptor of ORR activity on pristine, N- and B-doped CNTs. U_{eq}: equilibrium potential of 4e- ORR process. U_1 and U_4 represent the first and fourth ORR reaction steps; (c)-(e) are reproduced with permission.[166] Copyright 2020, Royal Society of Chemistry.

4. Carbon Materials in Fuel Cells

We summarise here in simply terms how carbon materials have been used in fuel cells. In membrane electrode assemblies for transportation applications, the Pt-utilization and the cost targets for 2020, as defined by the U.S. Department of Energy (U.S. DOE), are 0.125 g.kW^{-1} and 14 \$.kW^{-1}, respectively.[179] The cost of the cathode can be 36-56% of the total for a fuel cell because of the significant amount of Pt-based catalyst present[180,181] and despite Pt-based electrocatalysts often suffering from poor stability, fuel crossover and gas poisoning effects.[5,182]

Table 2. A comparison of different carbon materials in fuel cells.

Materials	**Condition**	**Maximum power density**	**Electron transfer number**	**Ref.**
N-doped CNTs	acidic membrane, cathode loading 0.16 mg cm^{-2}, 80 °C	320 W g^{-1}, 51.2 mW cm^{-2}	4 in 0.1 M KOH	[185]
Partially unzipped CNTs	acidic membrane, cathode loading 0.25 mg cm^{-2}, 80 °C	520 W g^{-1}, 161 mW cm^{-2}	4 in 0.1 M KOH, 3.6-3.9 in 0.5 M H_2SO_4	[26]
N-doped hierarchical carbon	alkaline membrane, cathode loading 1 mg cm^{-2}, 70 °C	228 W g^{-1}, 228 mW cm^{-2}	3.94-4 in 0.1 M KOH	[25]
N-doped carbon nanohorn	alkaline membrane, cathode loading 0.2 mg cm^{-2}, 80 °C	127 W g^{-1}, 25.5 mW cm^{-2}	3.6 in 0.1 M KOH	[186]
NiCo-N doped CNTs	alkaline membrane, cathode loading 4 mg cm^{-2}	16.25 W g^{-1}, 65 mW cm^{-2}	4	[187]
Tridoped graphene	acidic membrane, cathode loading 1.5 mg cm^{-2}	9.33 W g^{-1}, 14 mW cm^{-2}	3.0 in 0.1 M NaOH	[183]
	alkaline membrane, cathode loading 1.5 mg cm^{-2}	30.65 W g^{-1}, 46 mW cm^{-2}	3.0 in 0.1 M NaOH	[183]
N-doped graphene	alkaline membrane, cathode loading 2 mg cm^{-2}, 60 °C	1.3 W g^{-1}, 2.6 mW cm^{-2}	3.75-3.95 in 0.1 M KOH	[188]
N-doped nanopores graphene	alkaline membrane, cathode loading 2.5 mg cm^{-2}, 50 °C	10.8 W g^{-1}, 27 mW cm^{-2}	2.9–3.7 in 1.0 M KOH	[189]
S-doped graphene	alkaline membrane, cathode loading 0.3 mg cm^{-2}, 95 °C	9.43 W g^{-1}, 2.83 mW cm^{-2}	2.0-2.5 in 0.1 M KOH	[190]

Carbon materials offer much promise for replacing Pt as the cathode material of fuel cells and achieving high stability while supporting ORR. **Table 2** summarises some key demonstrations of fuel cells with carbon-based electrodes and either acidic or alkaline membranes. Alkaline media is usually preferred for these electrode materials,[13,23,116] since this gives higher power densities than with acidic media.[26, 183,184] Fuel cell performance is governed by the cell layout and various efficiency parameters (*e.g.* ion transfer and mass transfer) as well as by the ORR activity and pathway of the cathode. The 4e$^-$ ORR process could offer higher current and power densities, than 2e$^-$ ORR, and so is more favorable in fuel cells. **Table 2** compares the maximum power density of various fuel cells assembled from different carbon cathodes. There is a clear trend of this power density increasing with the electrode transfer number.[25, 26, 185-190] N-doped graphene with a nearly-four-electron ORR pathway is an exceptional case in that it shows a particularly low maximum power density of 1.3 $W.g^{-1}$.[188] As we discussed above, graphene materials are more inert than CNTs for the ORR, without the contribution from geometic and topologic defects (*e.g.* curvature, highly corrugated surface, edges). The ORR electron transfer numbers of N-doped graphene and N-doped CNTs (around four) are likely to differ. Precise determination of the electron transfer number will be extremely important for guiding the development of carbon-based materials for particular applications (*e.g.* fuel cells or the production of H_2O_2). A rotating ring-disk electrode (RRDE) is useful in determing the electron transfer number involved in the ORR catalysis. Nevertheless, as we explained above, the collection efficiency of the ring electrode is not always steady and should be calibrated appropriately before any measurements are taken. Direct measurement of H_2O_2 production from the electrolyte could also be used to verify the RRDE data. The ORR resulting from use of glassy carbon electrodes can be considered as a result of using defected structures, which should be avoided in any precise evaluation of the selectivity. We suggest, if possible, using either a rotating disk electrode (RDE) or rotating ring-disk electrode (RRDE) with only the basal plane of a HOPG disk exposed.

5. Conclusions and Prospects

The low cost, electrochemical stability and strong catalytic performance of carbon-based materials makes them promising candidates for replacing precious metals in electrochemical ORR. Here, we have summarized recent progress in engineering carbon materials towards supporting improved ORR efficiency. Although the detailed electrochemical mechanisms involving different engineered carbon materials are still yet to be further understood, recent progress suggests key issues for consideration that could yield improved ORR performance. These include that:

- catalytic activity and selectivity of carbon materials are in part dependent on their chemical affinity to O_2 of ORR intermediates, which can be tuned by chemical doping and defect engineering of the carbon materials;
- suitable chemical doping of carbon materials can change local charge distributions and the nature of local O_2 adsorption, thus enabling the C or dopant atoms to become catalytically-active sites;
- the distorted geometrical structures formed to accommodate dopant atoms with radii larger than that of a C atom can also result in charge redistribution and improve ORR activity;
- defect structures such as zigzag edges and re-constructured pentagon edges are highly active in ORR;
- other defects such as wrinkles, corrugations, vacancies, strain and curvature in the surfaces of carbon materials should be considered as important contributors to ORR catalyst performance.

Among various dopants, N has so far been shown to be the most powerful element to regulate the electronic structure of carbon materials and, thereby, to enable the highest ORR activity. Understanding the effect of doping on chemical affinity can be established using the orbital hybridization model proposed by Qiao *et al.* (**Figure 4i**).[113] To improve the binding ability of carbon materials to ORR intermediates, the valence orbital energy of the active site should be increased. This model also explained various observations of defected structures of carbon materials improving the ORR activity, by enhancing the LDOS at the Fermi level and lifting the valance bands.

However, it is still highly challenging to understand the exact effects of various defects on the ORR activity and selectivity. The chemical affinity of carbon materials is highly dependent on defect position, defect type, and wider geometric and topological structures, the latter two of which can also be treated as types of defects to improve the LDOS. The ORR electron transfer number has been found to range between 2.9 and 4 in different carbon materials,[13,23,26] implying that the activation and regulation of ORR from a 2e$^-$ to a 4e$^-$ pathway is possible. The defect-dependent chemical affinity and ORR activity also explains why so many engineered carbon materials (*e.g.* CNTs, graphene, activated carbon materials and particles) have different reaction pathways and activities.[13,30,52,54,56,57,58,60-64] In any future designs and investigations of carbon-based ORR catalysts, all of these defects, and not just re-constructed pentagon carbon rings, should all be considered, e.g. in DFT simulations.

This analysis suggests possible carbon materials with both defected structures and chemical doping beyond just N-doped CNTs to support the 4e$^-$ ORR used in fuel cells and energy storage devices (*e.g.* Zn-air batteries). The 4e$^-$ ORR is achievable using partially-unzipped CNTs as catalysts (electron transfer number ranging from 3.6 – 3.9), although detailed structural information of, for example, bond lengths and defects of the nanoribbons needs to be clarified to explain the higher binding ability over that required by the 2e$^-$ pathway. Undoped carbon materials with well-controlled defect levels are also suggested for the production of H_2O_2. These carbon materials can include carbon cloth, carbon paper and graphene-based composites with robust mechanical strength. Unfortunately, research on such undoped defected carbon materials for 2e$^-$ ORR is not widely reported and there remains scientific debate on the effect of CNT curvature upon ORR activity and selectivity. Although the chemical binding ability of pure CNTs is still unclear, the activation and selection regulation of ORR may be possible using CNTs with different curvature by combing various defected structures, such as lattice dislocations and point defects.[166-178]

This work shows that future research that considers the structure, defect-state and composition of carbon materials alongside the consideration of experimental arrangements may see significant improvements in their effectiveness as catalysts for the ORR. Indeed, similar principles are likely to see the development of robust carbon materials with tunable selectivity and performance for other reactions too, such as carbon dioxide reduction reaction (CO_2RR).

Acknowledgements

Financial supports from University of Wollongong Vice-Chancellor Fellowship, Australian Research Council Centre of Excellence Scheme (CE140100012), National Key Research and Development Program of China (2017YFB0701700) and the National Natural Science Foundation of China (61874146 and 21803005) are gratefully acknowledged. The authors would like to thank the Australian National Fabrication Facility - Materials node for facility access.

Conflict of Interest

The authors declare no conflict of interest.

Received: ((will be filled in by the editorial staff))
Revised: ((will be filled in by the editorial staff))
Published online: ((will be filled in by the editorial staff))

References

[1] M. Li, X. Bi, R. Wang, Y. Li, G. Jiang, L. Li, C. Zhong, Z. Chen, J. Li, *Matter* **2020**, 2, 31.

[2] S. Siahrostami, A. Verdaguer-Casadevall, M. Karamad, D. Deiana, P. Malacrida, B. Wickman, M. Escudero-Escribano, E. A. Paoli, R. Frydendal, T. W. Hansen, Ib Chorkendorff, I. E. L. Stephens, J. Rossmeisl, *Nat. Mater.* **2013**, 12, 1137.

[3] Q. Chang, P. Zhang, A. H. B. Mostaghimi, X. Zhao, S. R. Denny, J. H. Lee, H. Gao, Y. Zhang, H. L. Xin, S. Siahrostami, J. G. Chen, Z. Chen, *Nat. Commun.* **2020**, 11, 2178.

[4] Z. Zhao, M. D. Hossain, C. Xu, Z. Lu, Y.-S. Liu, S.-H. Hsieh, I. Lee, W. Gao, J. Yang, B. V. Merinov, W. Xue, Z. Liu, J. Zhou, Z. Luo, X. Pan, F. Zaera, J. Guo, X. Duan, W. A. Goddard III, Y. Huang, *Matter* **2020**, 3, 1774.

[5] R. Ma, G. Lin, Y. Zhou, Q. Liu, T. Zhang, G. Shan, M. Yang, J. Wang, *npj Comput. Matter.* **2019**, 5, 78.

[6] L. Cao, Z. Zhao, Z. Liu, W. Gao, S. Dai, J. Gha, W. Xue, H. Sun, X. Duan, X. Pan, T. Mueller, Y. Huang, *Matter* **2019**, 1, 1567.

[7] L. Chen, Q. Xu, *Matter* **2019**, 1, 57.

[8] N. Zhang, T. Zhou, J. Ge, Y. Lin, Z. Du, C. Zhong, W. Wang, Q. Jiao, R. Yuan, Y. Tian, W. Chu, C. Wu, Y. Xie, *Matter* **2020**, 3, 509.

[9] Y. Li, Q. Li, H. Wang, L. Zhang, D. P. Wilkinson, J. Zhang, *Electrochem. Energy Rev.* **2019**, 2, 518.

[10] J. Liu, M. Jiao, L. Lu, H. M. Barkholtz, Y. Li, Y. Wang, L. Jiang, Z. Wu, D. Liu, L. Zhuang, C. Ma, J. Zeng, B. Zhang, D. Su, P. Song, W. Xing, W. Xu, Y. Wang, Z. Jiang, G. Sun, *Nat. Commun.* **2017**, 8, 15938.

[11] K. Jiang, S. Back, A. J. Akey, C. Xia, Y. Hu, W. Liang, D. Schaak, E. Stavitski, J. K. Nørskov, S. Siahrostami, H. Wang, *Nat. Commun.* **2019**, 10, 3997.

[12] Z.-F. Huang, J. Song, S. Dou, X. Li, J. Wang, X. Wang, *Matter* **2019**, 1, 1494.

[13] K. Gong, F. Du, Z. Xia, M. Durstock, L. Dai, *Science* **2009**, 323, 760.

[14] K. F. L. Hagesteijn, S. Jiang, B. P. Ladewig, *J. Mater. Sci.* **2018**, 53, 11131.

[15] J. Durst, A. Siebal, C. Simon, F. Hasché., J. Herranz, H. A. Gasteiger, *Energy Environ. Sci.* **2014**, 7, 2255.

[16] D. R. Dekel, *J. Power Soruces* **2018**, 375, 158.

[17] L. Yang, S. Jiang, Y. Zhao. L. Zhu, S. Chen, X. Wang, Q. Wu, J. Ma, Y. Ma, Z. Hu, *Angew. Chem. Int. Ed.* **2011**, 50, 7132.

[18] X. Wang, G. Yang, G. Chai, M. S. Nasir, S. Wang, X. Zheng, C. Wang, W. Yan, *Int. J. Hydrogen Energ.* **2020**, 45, 30634.

[19] J. Zhang, L. Dai, *ACS Catal.* **2015**, 5, 7244.

[20] R. Kobayashi, T. Ishii, Y. Imashiro, J. Ozaki, *Beilstein J. Nanotechnol.* **2019**, 10, 1497.

[21] H. Tan, Y. Li, X. Jiang, J. Tang, Z. Wang, H. Qian, P. Mei, V. Malgras, Y. Bando, Y. Yamauchi, *Nano Energy* **2017**, 36, 286.

[22] J. Guo, J. Zhang, H. Zhao, Y. Fang, K. Ming, H. Huang, J. Chen, X. Wang, *R. Soc. Open Sci.* **2018**, 5, 5180925.

[23] Y. Jiang, L. Yang, T. Sun, J. Zhao, Z. Lyu, O. Zhou, X. Wang, Q. Wu, J. Ma, Z. Hu,

ACS Catal. **2015**, 5, 6707.

[24] Y. Liu, X. Quan, X. Fan, H. Wang, S. Chen, *Angew. Chem. Int. Ed.* **2015**, 127, 6941.

[25] J. W. F. To, J. W. D. Ng, S. Siahrostami, A. L. Koh, Y. Lee, Z. Chen, K. D. Fong, S. Chen, J. He, W.-G. Bae, J. Wilcox, H. Y. Jeong, K. Kim, F. Studt, J. K. Nørskov, T. F. Jaramillo, Z. Bao, *Nano Res.* **2017**, 10, 1163.

[26] L. Xue, Y. Li, X. Liu, Q. Liu, J. Shang, H. Duan, L. Dai, J. Shui, *Nat. Commun.* **2018**, 9, 3819.

[27] W. Wei, Y. Tao, W. Lv, F.-Y. Su, L. Ke, J. Li, D.-W. Wang, B. Li, F. Kang, Q.-H. Yang, *Sci. Rep.* **2014**, 4, 6289.

[28] B. Huang, P. Lu, F. Yang, Y. Liu, Z. Xie, *J. Energy Chem.* **2017**, 26, 712.

[29] Y. Cheng, H. Zhang, C. V. Varanasi, J. Liu, *Sci. Rep.* **2013**, 3, 3195.

[30] Q. Lv, W. Si, J. He, L. Sun, C. Zhang, N. Wang, Z. Yang, X. Li, X. Wang, W. Deng, Y. Long, C. Huang, Y. Li, *Nat. Commun.* **2018**, 9, 3376.

[31] H.-W. Liang, X. Zhuang, S. Brüller, X. Feng, K. Müllen, *Nat. Commun.* **2014**, 5, 4973.

[32] X. Sun, P. Song, Y. Zhang, C. Liu, W. Xu, W. Xing, *Sci. Rep.* **2013**, 3, 2505.

[33] J. Y. Cheon, T. Kim, Y. Choi, H. Y. Jeong, M. G. Kim, Y. J. Sa, J. Kim, Z. Lee, T.-H. Yang, K. Kwon, O. Terasaki, G.-G. Park, R. R. Adzic, S. H. Joo, *Sci. Rep.* **2013**, 3, 2715.

[34] A. Kulkarni, S. Siahrostami, A. Patel, J. K. Nørskov, *Chem. Rev.* **2018**, 118, 2302.

[35] H. A. Hansen, J. Rossmeisl, J. K. Nørskov, *Phys. Chem. Chem. Phys.* **2008**, 10, 3722.

[36] V. Viswanathan, H. A. Hansen, J. Rossmeisl, J. K. Norskov, *J. Phys. Chem. Lett.* **2012**, 3, 2948.

[37] S. Dey, B. Mondal, S. Chatterjee, A. Rana, S. Amanullah, A. Dey, *Nat. Rev. Chem.* **2017**, 1, 0098.

[38] J. K. Nørskov, J. Rossmeisl, A. Logadottir, L. Lindqvist, J. R. Kitchin, T. Bligaard, H. Jónsson, *J. Phys. Chem. B* **2004**, 108, 17886.

[39] J. K. Nørskov, F. Abild-Pedersen, F. Studt, T. Bilgaard, *Proc. Natl. Acad. Sci.* **2011**, 108, 937.

[40] A. A. Latimer, A. R. Kulkarni, H. Aljama, J. H. Montoya, J. S.Yoo, C. Tsai, F. Abild-Pedersen, J. K. Norskov, *Nat. Mater.* **2017**, 16, 225.

[41] J. K. Norskov, T. Bligaard, J. Rossmeisl, C. H. Christensen, *Nat. Chem.* **2009**, 1, 37.

[42] F.Abild-Pedersen, J. Greeley, F. Studt, J. Rossmeisl, T. R. Munter, P. G. Moses, E. Skulason, T. Bligaard, J. K. Norskov, *Phys. Rev. Lett.* **2007**, 99, 016105.

[43] V. Viswanathan, H. A. Hansen, J. Rossmeisl, J. K. Nørskov, *ACS Catal.* **2012**, 2, 1654.

[44] L. Lin, P. Sherrell, Y. Liu, W. Lei, S. Zhang, H. Zhang, G.G. Wallace, J. Chen, *Adv. Energy Mater.* **2020**, 10, 1903870.

[45] L. Lin, N, Miao, Y. Wen, S. Zhang, P. Ghosez, Z. Sun, D.A. Allwood, *ACS Nano* **2016**, 10, 8929.

[46] P. Vassilev, M. T. M. Koper, *J. Phys. Chem. C* **2007**, 111, 2607.

[47] L. Lin, J. Chen, D. Liu, X. Li, G. G. Wallace, S. Zhang, *Adv. Energy Mater.* **2020**, 10, 2002621.

[48] S.-H. Jhi, S. G. Louie, M. L. Cohen, *Phys. Rev. Lett.* **2000**, 85, 1710.

[48] S. Peng, K. Cho, *Nanotechnology* **2000**, 11, 57.

[49] J. Zhao, A. Buldum, J. Han, J. P. Lu, *Nanotechnology* **2002**, 13, 195.

[50] P. Giannozzi, R. Car, G. Scoles, *J. Chem. Phys.* **2003**, 118, 1003.

[51] R. G. A. Veiga, R. H. Miwa, G. P. Srivastava, *J. Chem. Phys.* **2008**, 128, 201101.

[52] R. Liu, D. Wu, X. Feng, K. Müllen, *Angew. Chem. Int. Ed.* **2010**, 49, 2565.

[53] L. Qu, Y. Liu, J.-B. Baek, L. Dai, *ACS Nano* **2010**, 4, 1321.

[54] C. V. Rao, C. R. Cabrera, Y. Ishikawa, *J. Phys. Chem. Lett.* **2010**, 1, 2622.

[55] H. Kim, K. Lee, S. I. Woo, Y. Jung, *Phys. Chem. Chem. Phys.* **2011**, 13, 17505.

[56] L. Lai, J. R. Potts, D. Zhan, L. Wang, C. K. Poh, C. Tang, H. Gong, Z. Shen, J. Lin, R. S. Ruoff, *Energy Environ. Sci.* **2012**, 5, 7936.

[57] W. Ding, Z. Wei, S. Chen, X. Qi, T. Yang, J. Hu, D. Wang, L. J. Wan, S. F. Alvi, L. Li, *Angew. Chem. Int. Ed.* **2013**, 52, 11755.

[58] T. Xing, Y. Zheng, L. H. Li, B. C. C. Cowie, D. Gunzelmann, S. Z. Qiao, S. Huang, Y. Chen, *ACS Nano* **2014**, 8, 6856.

[59] D. Guo, R. Shibuya, C. Akiba, S. Saji, T. Kondo, J. Nakamura, *Science* **2016**, 351, 361.

[60] R. Du, N. Zhang, J. Zhu, Y. Wang, C. Xu, Y. Hu, N. Mao, H. Xu, W. Duan, L. Zhuang, L. Qu, Y. Hou, J. Zhang, *Small* **2015**, 11, 3903.

[61] J. Quílez-Bermejo, M. Melle-Franco, E. San-Fabián, E. Morallón, D. Cazorla-Amorós, *J. Mater. Chem. A* **2019**, 7, 24239.

[62] M. Zhu, P. Xie, L. F. Fan, M. Z. Rong, M. Q. Zhang, Z. P. Zhang, *Nanotechnology* **2020**, 31, 335717.

[63] C. Guo, Z. Li, L. Niu, W. Liao, L. Sun, B. Wen, Y. Nie, J. Cheng, G. Chen, *Nanoscale Res. Lett.* **2016**, 11, 268.

[64] C. Guo, Z. Li, L. Niu, W. Liao, L. Sun, B. Wen, Y. Nie, J. Cheng, G. Chen, *Nanoscale Res. Lett.* **2016**, 11, 268.

[65] H. B. Yang, J. Miao, S.-F. Hung, J. Chen, H. B. Tao, X. Wang, L. Zhang, R. Chen, j. Gao, H. M. Chen, L. Dai, B. Liu, *Sci. Adv.* **2016**, 2, e1501122.

[66] M. Li, L. Zhang,Q. Xu, J. Niu, Z. Xia, *J. Catal.* **2014**, 314, 66.

[67] T. Wang, Z.-X. Chen, Y.-G. Chen, L.-J. Yang, X.-D. Yang, J.-Y. Ye, H.-P. Xia, Z.-Y. Zhou, S.-G. Sun, *ACS Energy Lett.* **2018**, 3, 986.

[68] L. Zhang, Z. Xia, *J. Phys. Chem. C* **2011**, 115, 11170.

[69] A. Ferre-Vilaplana, E. Herrero, *Electrochim. Acta* **2016**, 204, 245.

[70] Z. Yao, G. Henkelman, *J. Phys. Chem. C* **2020**, 124, 12016.

[71] T. Kondo, S. Casolo, T. Suzuki, T. Shikano, M. Sakurai, Y. Harada, M. Saito, M. Oshima, M. I. Trioni, G. F. Tantardini, J. Nakamura, *Phys. Rev. B* **2012**, 86, 035436.

[72] H. Metiu, S. Chrétien, Z. Hu, B. Li, X. Sun, *J. Phys. Chem. C* **2012**, 116, 10439.

[73] L. Lin, N. Xu, C. Wu, J. Huang, A. Nattestad, X. Zheng, G. G. Wallace, S. Zhang, J. Chen, *Matter* **2021**, 4, 955.

[74] A. Mashreghi, M. M. Moshksar, *Comput. Mater. Sci.* **2010**, 49, 871.

[75] S. Thompho, O. Saengsawang, T. Rungrotmongkol, N. Kungwan, S. Hannongbua, *Struct. Chem.* **2018**, 29, 39.

[76] D. Sanclez–Portal, E. Artacho, J.M. Soler, A. Rubio, P. Ordejon, *Phys. Rev. B* **1999**, 59, 12678.

[77] L. Lin. X. Zheng, S. Zhang, Dan A. Allwood, *Adv. Mater. Interfaces* **2014**, 1300078.

[78] L. Lin, L. Ma, S. Zhang, J. Hunag, Dan A. Allwood, *CrystEngComm* **2015**, 17, 1491.

[79] D. Chan, M. A. Hozbor, E. Bayramli, *Carbon*, **1991**, 29, 1091.

[80] Y. Zhao, L. Yang, S. Chen, X. Wang, Y. Ma, Q. Wu, Y. Jiang, W. Qian, Z. Hu, *J. Am. Chem. Soc.* **2013**, 135, 1201.

[81] S. Liu, G. Li, Y. Gao, Z. Xiao, J. Zhang, Q. Wang, X. Zhang, L. Wang, *Catal. Sci. Technol.* **2017**, 7, 4007.

[82] J.-C. Li, P.-X. Hou, C. Liu, *Small* **2017**, 13, 1702002.

[83] H. Tavakol, F. Keshavarzipour, *RSC Adv.* **2016**, 6, 63084.

[84] Q. Shi, F. Peng, S. Liao, H. Wang, H. Yu, Z. Liu, B. Zhang, D. Su, *J. Mater. Chem. A* **2013**, 1, 14853.

[85] G. Zhao, L. Shi, J. Xu, X. Yan. T. S. Zhao, *Int. J. Hydrogen Energy* **2018**, 43, 1470.

[86] L.-P. Yuan, Y.-Y. Wu, W.-J. Jiang, T. Tang, S. Niu, J.-S. Hu, *Nano Res.* **2020**, 13, 1376.

[87] T. Gong, R. Qi, X. Liu, H. Li, Y. Zhang, *Nano-Micro Lett.* **2019**, 11, 2714.

[88] D.-S. Yang, D. Bhattacharjya, S. Inamdar, J. Park, J.-S. Yu, *J. Am. Chem. Soc.* **2012**, 134, 16127.

[89] Y. Zhang, N. Huang, J. Zhang, S. Qiao, Y. Sun, Z. Gao, *ECS J. Solid State Sci.* **2018**, 7, M123.

[90] M. Wang, Y. Li, J. Fang, C. J. Villa, Y. Xu, S. Hao, J. Li, Y. Liu, C. Wolverton, X. Chen, V. P. Dravid, Y. Lai, *Adv. Energy Mater.* **2020**, 10, 1902736.

[91] Y. Zhang, N. Huang, S. Qiao, J. Zhang, Z. Gao, Z. Qiu, S. Zhou, X. Jiang, *Mod. Phus. Lett. B* **2019**, 33, 1950046.

[92] J. Wu, Z. Yang, X. Li, Q. Sun, C. Jin, P. Strasser, R. Yang, *J. Mater. Chem. A* **2013**, 1, 9889.

[93] J. Wu, Z. Yang, Q. Sun, X. Li, P. Strasser, R. Yang, *Electrochim. Acta* **2014**, 127, 53.

[94] Z. Liu, F. Peng, H. Wang, H. Yu, W. Zheng, X. Wei, *J. Nat. Gas Chem.* **2012**, 21, 257.

[95] X. Zhang, Z. Lu, Z. Fu, Y. Tang, D. Ma, Z. Yang, *J. Power Sources* **2015**, 276, 222.

[96] H.-M. Wang, H.-X. Wang, Y. Chen, Y.-J. Liu, K.-X. Zhao, Q.-H. Cai, X.-Z. Wang, *Appl. Surf. Sci.* **2013**, 273, 302.

[97] J. Rossmeisl, A. Logadottir, J.K. Nørskov, *Chem. Phys.* **2005**, 319,178.

[98] J. Rossmeisl, Z.-W. Qu, H. Zhu, G.-J. Kroes, J.K. Nørskov, *J. Electroanal. Chem.* **2007**, 607, 83.

[99] Y. Wang, W. Song, M. Li, Z. Wu, *J. Electrochem. Soc.* **2019**, 166, F670.

[100] J. Gao, J. Zhang, H. Zhao, Y. Fang, K. Min, H. Huang, J. Chen, X. Wang, *R. Soc. Open Sci.* **2018**, 5, 180925.

[101] T. Gong, R. Qi, X. Liu, H. Li, Y. Zhang, *Nano-Micro Lett.* **2019**, 11, 9.

[102] G. Panomsuwan, N. Saito, T. Ishizaki, *J. Mater. Chem. A* **2015**, 3, 9972.

[103] P. Zhang, X. Hou, J. Mi, Y. He, L. Lin, Q. Jiang, M. Dong, *Phys. Chem. Chem. Phys.* **2014**, 16, 17479.

[104] X. Fu, Q.-D. Wang, Z. Liu, F. Peng, *Mater. Lett.* **2015**, 158, 32.

[105] X. Sun, P. Song, T. Chen, J. Liu, W. Xu, *Chem. Commun.* **2013**, 49, 10296.

[106] X. Sun, Y. Zhang, P. Song, J. Pan, L. Zhuang, W. Xu, W. Xing, *ACS Catal.* **2013**, 3, 1726.

[107] I.-Y. Jeon, H.-J. Choi, M. Choi, J.-M. Seo, S.-M. Jung, M.-J. Kim, S. Zhang, L. Zhang,

Z. Xia, L. Dai, N. Park, J.-B. Baek, *Sci. Rep.* **2013**, 3, 1810.

[108] Z. Yao, H. Nie, Z. Yang, X. Zhou, Z. Liu, S. Huang, *Chem. Commun.* **2012**, 48, 1027.

[109] Z. Jin, H. Nie, Z. Yang, J. Zhang, Z. Liu, X. Xu, S. Huang, *Nanoscale* **2012**, 4 ,6455.

[110] I.-Y. Jeon, M. Choi, H.-J. Choi, S.-M. Jung, M.-J. Kim, J.-M. Seo, S.-Y. Bae, S. Yoo, G. Kim, H. Y. Jeong, N. Park, J.-B. Baek, *Nat. Commun.* **2015**, 6, 7123.

[111] Z. Zhao, M. Li, L. Zhang, L. Dai, Z. Xia, *Adv. Mater.* **2015**, 27, 6834.

[112] B. Hammer, J. K. Norskov, *Nature* **1995**, 376, 238.

[113] Y. Jiao, Y. Zheng, M. Jaroniec, S. Z. Qiao, *J. Am. Chem. Soc.* **2014**, 136, 4394.

[114] J. Liang, Y. Jiao, M. Jaroniec, S. Z. Qiao, *Angew. Chem. Int. Ed.* **2012**, 51, 11496.

[115] Y. Su, Z. Yao, F. Zhang, H. Wang, Z. Mics, R. Cánovas, M. Bonn, X. Zhuang, X. Feng, *Adv. Funct. Mater.* **2016**, 26, 5893.

[116] G. Yang, W. Choi, X. Pu, C. Yu, *Energy Environ. Sci.* **2015**, 8, 1799.

[117] J.-C. Li, X. Qin, P.-X. Hou, M. Cheng, C. Shi, C. Liu, H.-M. Cheng, M. Shao, *Carbon* **2019**, 147, 303.

[118] Y. Meng, D. Voiry, A. Goswami, X. Zou, X. Huang, M. Chhowalla, Z. Liu, T. Asefa, *J. Am. Chem. Soc.* **2014**, 136, 13554.

[119] X. Yan, H. Liu, Y. Jia, L. Zhang, W. Xu, X. Wang, J. Chen, D. Yang, X. Yao, *Cell Rep. Phys. Sci.* **2020**, 1, 100083.

[120] L. Tao, Q. Wang, S. Dou, Z. Ma, J. Huo, S. Wang, L. Dai, *Chem. Commun.* **2016**, 52, 2764.

[121] Q. Yang, Z. Xiao, D. Kong, T. Zhang, X. Duan, S. Zhou, Y. Niu, Y. Shen, H. Sun, S. Wang, L. Zhi, *Nano Energy* **2019**, 66, 104096.

[122] Z. Liu, Z. Zhao, Y. Wang, S. Dou, D. Yan, D. Liu, Z. Xia, S. Wang, *Adv. Mater.* **2017**, 29, 1607207.

[123] G. Liu, X. Li, B. Popov, *ECS Trans.* 2009, **25**, 1251.

[124] M. Rauf. Y.-D. Zhao, Y.-C. Wang, Y.-P. Zheng, C. Chen, X.-D. Yang, Z.-Y. Zhou, S.-

G. Sun, *Electrochem. Commun.* 2016, **73**, 71.

[125] D. Pan, J. Zhang, Z. Li, M, Wu, *Adv. Mater.* **2010**, 22, 734.

[126] L. Lin, S. Zhang, *Chem. Commun.* **2012**, 48, 10177.

[127] J. Chmiola, G. Yushin, Y. Gogotsi, C. Portet, P. Simon, P. L. Taberna, *Science* **2006**, 313, 1760.

[128] C. Zhang, L. Dai, *Chem* **2020**, 6, 1849.

[129] Y. Jia, L. Zhang, L. Zhuang, H. Liu, X. Yan, X. Wang, J. Liu, J. Wang, Y. Zheng, Z. Xiao, E. Taran, J. Chen, D. Yang, Z. Zhu, S. Wang, L. Dai, X. Yao, *Nat. Catal.* **2019**, 2, 688.

[130] D. Li, Y. Jia, G. Chang, J. Chen, H. Liu, J. Wang, Y. Hu, Y. Xia, D. Yang, X. Yao, *Chem* **2018**, 4, 2345.

[131] J. Zhu, Y. Huang, W. Mei, C. Zhao, C. Zhang, J. Zhang, I. S. Amiinu, S. Mu, *Angew. Chem. Int. Ed.* **2019**, 58, 3859.

[132] D. W. Boukhvalov, M. I. Katsnelson, *J. Phys. Chem. C* **2009**, 113, 14176.

[133] H. Pan, *Mater. Chem. Phys.* **2017**, 189, 111.

[134] M. A. Bissett, S. Konabe, S. Okada, M. Tsuji, H. Ago, *ACS Nano* **2013**, 7, 10335.

[135] S. Nigar, Z. Zhou, H. Wang, M. Imtiaz, *RSC Adv.* **2017**, 7, 51546.

[136] L. Zhao, Y. Li, G. Zhou, S. Lei, J. Tan, L. Lin, J. Wang, *Chinese Chem. Lett.* **2021**, 32, 900.

[137] L. Fan, S. Lei, H. M. K. Sari, L. Zhong, A. Kakimov, J. Wang, J. Chen, D. Liu, L. Huang, J. Hu, L. Lin, X. Li, *Nano Energy* **2020**, 78, 105235.

[138] B. J. Schultz, C. J. Patridge, V. Lee, C. Jaye, P. S. Lysaght, C. Smith, J. Barnett, D. A. Fischer, D. Prendergast, S. Banerjee, *Nat. Commun.* **2011**, 2, 372.

[139] H. Pan, B. Chen, *Sci. Rep.* **2014**, 4, 4198.

[140] D. Voiry, H. Yamaguchi, J. Li, R. Silva, D. C. B. Alves, T. Fujita, M. Chen, T. Asefa, V. B. Shenoy, G. Eda, M. Chhowalla, *Nat. Mater.* **2013**, *12*, 850.

[141] H. Li, C. Tsai, A. L. Koh, L. Cai, A. W. Contryman, A. H. Fragapane, J. Zhao, H. S. Han, H. C. Manoharan, F. Abild-Pedersen, J. K. Nørskov, X. Zheng, *Nat. Mater.* **2016**, *15*, 48.

[142] B. Yildiz, *MRS Bull.* **2014**, *39*, 147.

[143] L. Lin, N. Miao, J. Huang, S. Zhang, Y. Zhu, D. W. Horsell, P. Ghosez, Z. Sun, D. A. Allwood, *Nano Energy* **2017**, 38, 544.

[144] W. W. Gibbs, *Science* **2019**, 366, 6467.

[145] Y. Wang, R. Yang, Z. Shi, L. Zhang, D. Shi, E. Wang, G. Zhang, *ACS Nano* **2011**, 5, 3645.

[146] C. Hofer, C. Kramberger, M. E. A. Monazam, C. Mangler, A. Mittelberger, G. Argentero, J. Kotakoski, J. C. Meyer, *2D Mater.* **2018**, 5, 045029.

[147] A. Rossi, S. Piccinin, V. Pellegrini, S. Gironcoli, V. Tozzini, *J. Phys. Chem. C* **2015**, 119, 7900.

[148] L. Cao, M. Yang, Z. Lu, H. Pan, *Sci. China Mater.* **2017**, 60, 739.

[149] J. Zhang, Z. Wang, Z. Zhu, *J. Mol. Model.* **2013**, 19, 5515.

[150] J. C. Meyer, C. Kisielowski, R. Erni, M. D. Rossell, M. F. Crommie, A. Zettl, *Nano Lett.* **2008**, 8, 3582.

[151] F. Banhart, J. Kotakoski, A. V. Krasheninnikov, *ACS Nano* **2011**, 5, 26.

[152] M. M. Ugeda, I. Brihuega, F. Guinea, J. M. Gómez-Rodríguez, *Phys. Rev. Lett.* **2010**, 104, 096804.

[153] J. H. Warner, E. R. Margine, M. Mukai, A. W. Robertson, F. Giustino, A. I. Kirkland, *Science* **2012**, 337, 209.

[154] L. Vicarelli, S. J. Heerema, C. Dekker, H. W. Zandbergen, *ACS Nano* **2015**, 9, 3428.

[155] J. T. Robinson, M. K. Zalalutdinov, C. D. Cress, J. C. Culbertson, A. L. Friedman, A. Merrill, B. J. Landi, *ACS Nano* **2017**, 11, 4745.

[156] J. Lu, Y. Bao, C. L. Su, K. P. Loh, *ACS Nano* **2013**, 7, 8350.

[157] F. Mehmood, R. Pachter, W. Lu, J. J. Boeckl, *J. Phys. Chem. C* **2013**, 117, 10366.

[158] A. S. Kochnev, N. F. Morozov, I. A. Ovid'ko, B. N. Semenov, *Dokl. Phys.* **2016**, 61, 403.

[159] J. Kotakoski, A. V. Krasheninnikov, U. Kaiser, J. C. Meyer, *Phys. Rev. Lett.* **2011**, 106, 105505.

[160] L. Zhang, Q. Xu, J. Niu, Z. Xia, *Phys. Chem. Chem. Phys.* **2015**, 17, 16733.

[161] K. Y. Perez-Salcedo, S. Ruan, J. Su, X. Shi, A. M. Kannan, B. Escobar, *J. Porous Mater.* **2020**, 27, 959.

[162] X. Yan, Y. Jia, T. Odedairo, X. Zhao, Z. Jin, Z. Zhu, X. Yao, *Chem. Commun.* **2016**, 52, 8156.

[163] Y. Jia, L. Zhang, A. Du, G. Gao, J. Chen, X. Yan, C. L. Brown, X. Yao, *Adv. Mater.* **2016**, 28, 9532.

[164] S. Gotovac, H. Honda, Y. Hattori, K. Takahashi, H. Kanoh, K. Kaneko, *Nano Lett.* **2007**, 7, 583.

[165] H. Sha, R. Faller, *Phys. Chem. Chem. Phys.* **2016**, 18, 19944.

[166] K. Yang, J. Zaffran, B. Yang, *Phys. Chem. Chem. Phys.* **2020**, 22, 890.

[167] M. U. Kahaly, U. V. Waghmare, *B. Mater. Sci.* **2008**, 31, 335.

[168] F. J.Pérez-Alonsoa, M. A. Salamb, T. Herranza, J. L.Gómez de la Fuentea, S. A. Al-Thabaiti, S. N. Basahel, M. A. Peñaa, J. L. G. Fierroa, S. Rojas, *J. Power Sources* **2013**, 240, 494.

[169] X. Wang, Q. Li, H. Pan, Y. Lin, Y. Ke, H. Sheng, M. T. Swihart, G. Wu, *Nanoscale* **2015**, 7, 20290.

[170] S. Lei, B. Paulus, S. Li, B. Schmidt, *J. Comput. Chem.* **2016**, 37, 1313.

[171] Y.-F. Zhang, Z.-F. Liu, *J. Phys. Chem.* **2004**, 108, 11435.

[172] J. Moreno, S. Aspera, M. David, H. Kasai, *Carbon* **2015**, 936.

[173] P. G. Collins, K. Bradley, M. Ishigami, A. Zettl, *Science* **2000**, 287, 1801.

[174] P. J. Britto, K. S. V. Santhanam, A. Rubio, J. A. Alonso, P. M. Ajayan, *Adv. Mater.* **1999**, 11, 154.

[175] Y. Miyata, T. Kawai, Y. Miyamoto, K. Yanagi, Y. Maniwa, H. Kataura, *J. Phys. Chem. C* **2007**, 111, 9671.

[176] A. B. Silva-Tapia, X. Carcía-Carmona, L. R. Radovic, *Carbon* **2012**, 50, 1152.

[177] R. C. Haddon, *J. Am. Chem. Soc.* **1986**, 108, 2837.

[178] R. C. Haddon, *Science* **1993**, 261, 1545.

[179] DOE Technical Targets for Polymer Electrolyte Membrane Fuel Cell Components. https://www.energy.gov/eere/fuelcells/doe-technical-targets-polymer-electrolyte-membrane-fuel-cell-components.

[180] B. D. James, J. A. Kalinoski, in U.S. Department of Energy Hydrogen Program, **2008** Annual Progress Report, http://www.hydrogen.energy.gov/pdfs/progress08/v_a_2_james.pdf.

[181] F. Jaouen, E. Proietti, M. Lefèvre, R. Chenitz, J.-P. Dodelet, G. Wu, H. T. Chung, C. M. Johnston, P. Zelenay, *Energy Environ. Sci.* **2011**, 4, 114.

[182] J. Zhang, Z. Xia, L. Dai, *Sci. Adv.* **2015**, 1, e1500564.

[183] C. V. Pham, M. Klingele, B. Britton, K. R. Vuyyuru, T. Unmuessig, S. Holdcroft, A. Fisher, S. Thiele, *Adv. Sustainable Syst.* **2017**, 1, 1600038.

[184] L. Yang, J. Shui, L. Du, Y. Shao, J. Liu, L. Dai, Z. Hu, *Adv. Mater.* **2019**, 31, 1804799.

[185] J. Shui, M. Wang, F. Du, L. Dai, *Sci. Adv.* **2015**, 1, e1400129.

[186] S. M. Unni, S. N. Bhange, R. Illathvalappil, N. Mutneja, K. R. Patil, S. Kurungot, *Small* **2015**, 11, 352.

[187] S. Hanif, N. Iqbal, X. Shi, T. Noor, G. Ali, A.M. Kannan, *Renew. Energ.* **2020**, 154, 508.

[188] M. P. Kumar, M. M. Raju, A. Arunchander, S. Selvaraj, G. Kalita, T. N. Narayanan, A. K. Sahu, D. K. Pattanayak, *J. Electrochem. Soc.* **2016**, 163, F848.

[189] N. Tachibana, S. Ikeda, Y. Yukawa, M. Kawaguchi, *Carbon* **2017**, 115, 515.

[190] M. Klingele, C. Pham, K. R. Vuyyuru, B. Britton, S. Holdcroft, A. Fischer, S. Thiele, *Electrochem. Commun.* **2017**, 77, 71

TOC

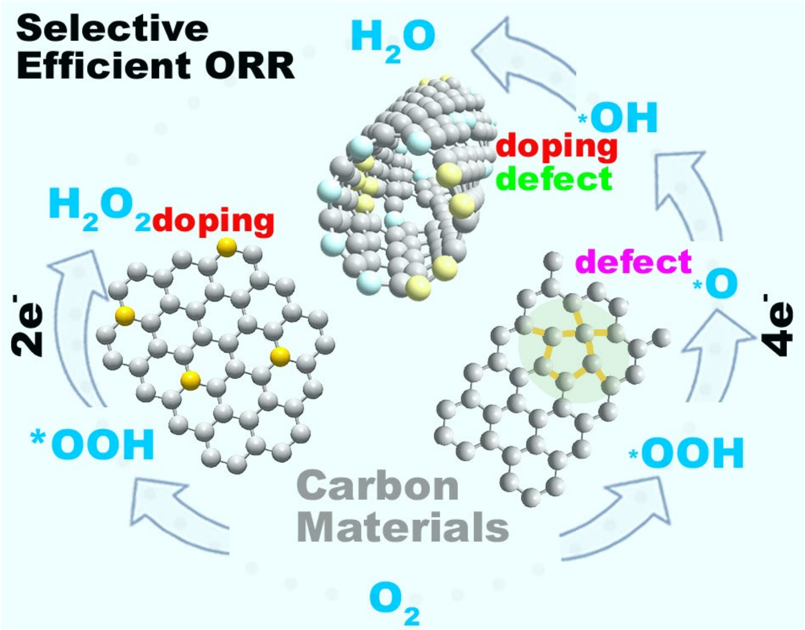

Building on fundamental understandings of the electrochemical oxygen reduction reaction, the key enginering strategies of carbon materials for the improved ORR are critically reviewed, providing clear and straightforward pathways towards the improved ORR with regulable activity and selectivity.

Liangxu Lin is currently a Vice-Chancellor Fellow at the University of Wollongong. He completed his PhD in Engineering Materials at The University of Sheffield at 2014. After two postdoc periods at the University of Exeter, he joined Wuhan University of Science and Technology as a Professor. He has a long-term research focus on 2D nanomaterials and interfaces for electrochemical energy storage/conversion, catalysis and device applications, from fundamental science to enginnering techniques.

Naihua Miao is an Associate Professor in the School of Materials Science and Engineering at Beihang University, Beijing, China. He received his B. Sc. (2008) and M. Sc. (2011) in materials science from Xiamen University (China), and a Ph.D. (2015) in condensed matter physics from the University of Liege (Belgium). His research interest includes the development of theoretical methodologies based on quantum mechanics and artificial intelligence, and their applications in the discovery of new advanced (bulk and 2D) materials.

Gordon Wallace is currently the executive research director/Professor at the ARC Centre of Excellence for Electromaterials Science, director of the Australian National Fabrication Facility (Materials Node), and Director of the Intelligent Polymer Research Institute (Australia). He previously held an ARC Federation Fellowship and currently holds an ARC Laureate Fellowship. His research interests include organic conductors, nanomaterials and electrochemical probe methods of analysis, and the use of these in the development of intelligent polymer systems.

Jun Chen is currently a Full Professor at IPRI|ACES, Australian Institute for Innovative Materials, University of Wollongong (UOW). He received BE from Zhejiang University of Technology (1995) and PhD from UOW (2003), and published more than 180 papers. His research interests include sustainable energy devices, electro-/bio-interfaces, nano-/micromaterials, 2D/3D printing, and smart wearable electronic devices. Apart from academic achievements, Chen has also been involved in two spin-off companies: AQUAHYDREX as one of the key inventors, and IMAGINE as one of the scientific founders.

Dan Allwood is a Full Professor at the Department of Materials Science and Enginering, University of Sheffield. He received BSc (1994) and PhD (1998) in Applied Physics from the University of Hull. His post-doctoral research posts were at University of Oxford, Imperial College London and Durham University. He moved to Sheffield for his EPSRC Advanced Research Fellowship in 2005. His has a research focus on the nanoscale magnetism, magneto-optics, and fundamental materials science (2D materials).